TÜBİTAK

Turkish Journal of Earth Sciences

http://journals.tubitak.gov.tr/earth/

Research Article

Turkish J Earth Sci
(2013) 22: 485-522
© TÜBİTAK
doi:10.3906/yer-1204-10

Low-sulfidation epithermal Au-Ag mineralization in the Sındırgı District, Balıkesir Province, Turkey

Hüseyin YILMAZ[1,*], Fatma Nuran SÖNMEZ[1], Erhan AKAY[1], Ahmet Kerim ŞENER[2], Seda TEZEL TUFAN[1]

[1]Dokuz Eylül University, Faculty of Engineering, Department of Geological Engineering, Buca, 35160 İzmir, Turkey

[2]Galata Madencilik Sanayi ve Ticaret Limitet Şirketi, Farabi Sokak No: 7/5, Çankaya, 06680 Ankara, Turkey

Received: 20.04.2012 • **Accepted:** 30.09.2012 • **Published Online:** 13.06.2013 • **Printed:** 12.07.2013

Abstract: The Sındırgı District (Balıkesir, western Turkey) lies within the Western Anatolian volcanic and extensional province, adjacent to the WNW-trending Simav graben, approximately 130 km NE of İzmir. The Sındırgı mining district is underlain mainly by Miocene volcanic rocks and hosts several low-sulfidation epithermal Au-Ag deposits and prospects located near the towns of Sındırgı and Bigadiç. The Kızıltepe low-sulfidation epithermal gold-silver deposit is located southeast of Yusufçam village (Sındırgı, Balıkesir), and other prospects, including the Kepez, Kavaklıdüz, and Karadüz prospects, are located northeast of Kızıltepe. Potentially economic grades occur at Kızıltepe, which contains a measured and indicated resource of 1.754.790 Mt @3.0 g/t Au, 44 g/t Ag, hosted by quartz veins showing colloform/crustiform banding, quartz pseudomorphs after bladed calcite, and multiphase brecciations, all typical textures noted in low-sulfidation epithermal deposits. Alteration minerals include mixed-layer illite/smectite, high-crystallinity illite, and kandite group minerals (dickite and nacrite). Precious metal minerals include traces of electrum, acanthite, Au-rich acanthite, and Ag-Hg-Au-Tl-Pb series, occurring mainly within quartz. Pyrite is the most common opaque mineral at Kızıltepe. $^{40}Ar/^{39}Ar$ dating of adularia from the quartz veins indicates an age of mineralization of 18.3 ± 0.2 Ma. The ore mineralization is divided into three main phases. These comprise the deposition of: coarse-grained quartz, illite, pyrite, and minor precious metals (Phase I); major gold–silver-bearing medium-grained quartz, which commonly exhibits crustiform banding, carbonate replacement, and hydrothermal breccia textures (Phase II); and fine-grained chalcedonic quartz with colloform/crustiform banding (Phase III). Phase II is economically the most important in terms of precious metal content. Phase II quartz contains fluid inclusions, which range from predominantly vapor-rich to predominantly liquid-rich with homogenization temperatures (Th) varying from 157 to 330 °C, showing a cluster between 190 and 300 °C, and ice-melting temperatures (Tm) ranging from –0.2 to –2.9 °C (salinity from 0.5-4.8 wt.% NaCl equiv.). Moderate to strong positive correlations occur between Au-Ag (R = 0.8) and Au-Cu (R = 0.5), whereas there is no correlation between As and Au or Ag.

Key words: Gold, hydrothermal alteration, geochronology, fluid inclusions, Sındırgı

1. Introduction

The Kızıltepe Au-Ag deposit and the Kepez, Kavaklıdüz, and Karadüz Au-Ag prospects (hereafter called the prospects, unless otherwise stated) are hosted in volcanic rocks that are part of the western Turkey magmatic arc complex related to the northward-dipping subduction and subsequent extension system of Neo-Tethys. The Eocene to Pliocene magmatic rocks consist of andesite, rhyolite, and latite lavas and volcaniclastic sequences of calc-alkaline to alkaline composition. They are tectonically linked to episodes of subduction, collision, and extension related to the northward movement of the African-Arabian plate (Ercan *et al.* 1984; Yılmaz 1989; Ercan *et al.* 1995; Pirajno 1995; Aldanmaz *et al.* 2000; Altunkaynak & Dilek 2006; Altunkaynak & Genç 2008). This magmatic arc complex in western Turkey constitutes a part of the Tethyan Eurasian Metallogenic Belt within the Alpine-Himalayan orogenic system that has been forming from the Jurassic–Cretaceous to the present (Yiğit 2006; Yiğit 2009). The Sındırgı district, which contains the Kızıltepe Au-Ag deposit and the Kepez, Kavaklıdere, and Karadüz Au-Ag prospects, is located almost centrally within this magmatic domain (Figure 1).

After the Ovacık and Küçükdere vein deposits (Çolakoğlu 2000; Yılmaz 2002, 2004; Yılmaz *et al.* 2007), the Kızıltepe Au-Ag deposit is one of the best examples of quartz-adularia low-sulfidation epithermal gold mineralization in the Western Anatolian Volcanic and Extensional (WAVE) province (Figure 1; Oygur 1997; Şener *et al.* 2006; Aysun & Çolakoğlu 2008). The WAVE province hosts several other epithermal and porphyry intrusion-related Au deposits (Yılmaz 2002; Yılmaz *et*

* Correspondence: huseyin.yilmaz@deu.edu.tr

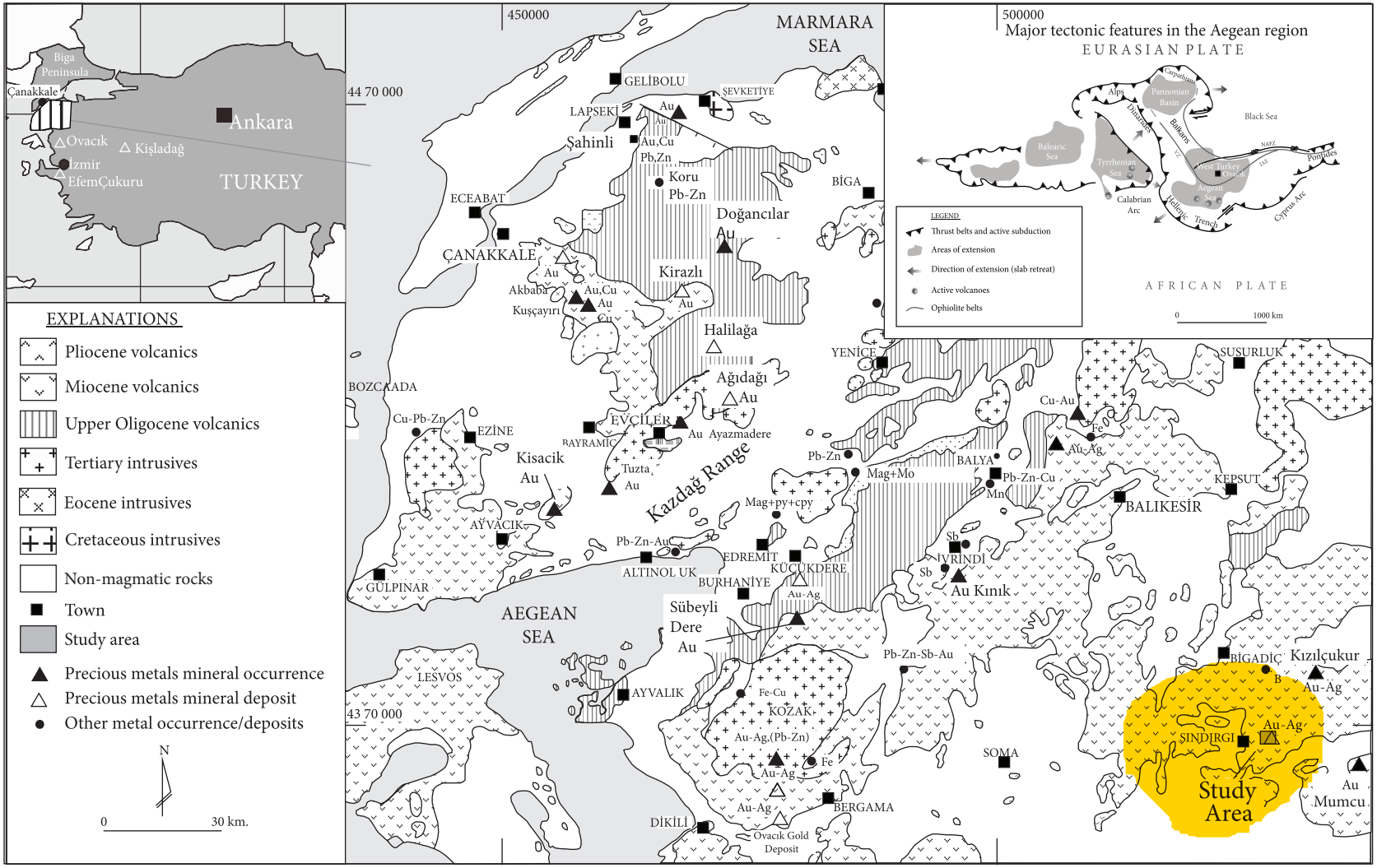

Figure 1. Simplified geological map of the Tertiary volcanic and plutonic field of northwest Turkey and location of the study area and areas of significant mineralization (volcanic and plutonic fields are modified from Ercan *et al.* 1984, 1995; Erkül *et al.* 2005; Tokçaer *et al.* 2005; Aldanmaz 2006).

al. 2007; 2010; Yiğit 2009), such as the low-sulfidation deposits (resource: measured and indicated) at Ovacık (4.19 Mt @ 7.6 g/t Au), Efemçukuru (4.09 Mt @ 11.0 g/t Au), and Küçükdere (1.27 Mt @ 6.4 g/t Au) and the porphyry intrusion-related deposit at Kışladağ (255 Mt @ 0.9 g/t Au).

The Kızıltepe deposit is classified as a quartz ± calcite ± adularia ± illite type (Simmons *et al.* 2005) or 'low-sulfidation' gold deposit based on wall-rock and vein alteration assemblages (Şener *et al.* 2006), and it is similar to several deposits elsewhere in the world, namely McLaughlin (Sherlock 2005), Golden Cross (Cooke & Simmons 2000; Simmons 2000), Pajingo (Dong *et al.* 1995), Hishikari (Hedenquist *et al.* 1996), and Adatepe (Marchev *et al.* 2004). This paper presents an integrated geological, alteration, geochronological, geochemical, and fluid inclusion study of the Kızıltepe deposit and related prospects, which represent the best-documented low-sulfidation occurrences in the Sındırgı District. The only recent studies on the occurrence of epithermal deposits in this region are papers by Oygur (1997), Şener *et al.* (2006), and Aysun and Çolakoğlu (2008), who documented the Mumcu prospect and Kızıltepe epithermal Au-Ag deposit, respectively. The paper by Şener *et al.* (2006) deals mainly with geological and macro-textural studies of the Kızıltepe deposit. The goal of the present investigation was to constrain the origin and evolution of the deposit in order to address fundamental questions regarding the temporal and spatial relationship between volcanism, adularia-illite alteration, and Au-Ag mineralization. The results of the study may be used in exploration for similar epithermal deposits in the Sındırgı District.

2. Mining and exploration history

Mining in the Sındırgı District started at the Kepez and Kızılçukur (also known as Derinin Tepe) gold prospects during Roman times. These gold occurrences occur at higher elevations (900 and 1400 m, respectively) than Kızıltepe (360 m). Substantial ancient mine workings and dumps were developed at Kızılçukur, particularly within a 1500-m-long epithermal vein. Pottery and millstones from shallow pits, shafts, and drives provide evidence that Au-Ag from epithermal quartz veins in the Sındırgı mining district was probably exploited since at least the Byzantine era (approximately 400 AD). The Sındırgı District gold deposits, including the Kızıltepe deposit, were discovered in modern times during a regional bulk leach extractable gold (BLEG) and 180-µm stream-sediment sampling program, undertaken in two separate phases between 1990 and 1992 by EuroGold (Yılmaz 1992) and TÜPRAG. During the initial BLEG sampling program by EuroGold, several anomalous gold values ranging up to 5 ppb Au were returned. Follow-up of the 5 ppb BLEG Au anomaly by 180-µm stream sediment, rockchip, and soil sampling in 1992 resulted in the discovery of the Kızıltepe and other prospects from the abundant epithermal quartz vein float. During further prospecting, over 50 km of several LS epithermal gold-bearing quartz veins were located in the Sındırgı District. Since 2005, approximately 20,000 m of drilling has been undertaken by Galata Madencilik San. & Tic. Ltd., the Turkish subsidiary of Ariana Resources plc on and around the deposit area during definition of the Kızıltepe Au-Ag deposit. In 2012, the Kızıltepe deposit contained a measured and indicated mineral resource of 168,245 oz Au, 2,479,211 oz Ag (Edison Investment Research update on Kızıltepe gold-silver deposit produced for Ariana Resources plc, 2011) or a total resource of 2,111,847 Mt containing 2.8 g/t Au and 44 g/t Ag.

3. Geological setting

3.1. Regional geology

Widespread magmatism occurred in western Turkey from the Late Oligocene to Early Miocene (Ercan *et al.* 1984; Yılmaz 1989; McKenzie & Yılmaz 1991; Seyitoğlu & Scott 1991; Seyitoğlu *et al.* 1997; Delaloye & Bingöl 2000; Yılmaz *et al.* 2001; Seyitoğlu *et al.* 1997; Altunkaynak & Yılmaz 1998; Akay & Erdoğan 2001, 2004; Yılmaz & Karacık 2001; Yılmaz *et al.* 2001; Erkül 2004; Erkül *et al.* 2005a, 2005b; Dilek & Altunkaynak 2007). Two magmatic episodes are distinguished, with an initial intermediate to felsic calc-alkaline magmatism during the Oligocene-Early Miocene (Yılmaz *et al.* 2001), when the granitic-granodioritic Kozak, Evciler, Ezine, Koyunoba, and Eğrigöz plutons were intruded at shallow levels in the crust (approximately 4 km below surface) during N-S-directed compression (Altunkaynak & Yılmaz 1998; Genç 1998; Karacık & Yılmaz 1998; Akay 2009; Hasözbek *et al.* 2012). The magmatic rocks of this phase are commonly high-K, calc-alkaline, and partly shoshonitic in nature (Yılmaz *et al.* 2001). Calc-alkaline to alkaline andesitic to rhyolitic lavas, domes, and pyroclastics accompany the plutonic phases between İzmir, Çanakkale, and Balıkesir (Figure 1). Altunkaynak and Yılmaz (1998) suggested that sheeted intrusions utilized NE-SW- and N-S-trending oblique faults to reach the surface. The compositions suggest crystallization from mantle-derived magmas contaminated by abundant crustal components (Yılmaz *et al.* 2001). Based on the geological and geochemical signature of these magmatic associations, similar to that of arc-derived associations, this magmatic event was regarded by Yılmaz *et al.* (2001) as the Tibetan type. The second magmatic phase consists of sporadically developed alkaline basalts (e.g., Kula basalts), which were emplaced from latest Miocene-Pliocene to recent time (Seyitoğlu *et al.* 1997).

Western Anatolia is one of the most seismically active and rapidly extending regions in the world; the crust in

this region is currently experiencing approximately N-S extension at a rate of 30-40 mm/year (Bozkurt 2003). Approximately E-W-trending grabens (e.g., the Edremit, Bakırçay, Kütahya, Simav, Gediz, Küçük Menderes, Büyük Menderes, and Gökova grabens) and their active basin-bounding normal faults are the most prominent neotectonic features of western Turkey (Bozkurt 2003). Other less prominent structural elements of western Turkey include the NNE-trending basins and intervening horsts (e.g., the Gördes, Demirci, Selendi, Cumaovası, and Uşak-Güre basins), which provide local structural controls on epithermal mineralizations (Yılmaz 2002; Yılmaz *et al.* 2007), as demonstrated at the Ovacık, Efemçukuru, and Kışladağ gold deposits (Figure 1).

During the Neogene, western Turkey was affected by several extensional events (Zanchi *et al.* 1990, 1993; Bozkurt 2003). The earliest (NW-SE) extensional phase, which prevailed from Middle to Late Miocene, gave rise to NNE-SSW- to NE-SW-trending graben, followed by N-S extension during the Early Pliocene to Quaternary. The deposition of overlying Upper Miocene-Lower Pliocene sedimentary successions was restricted to NE-SW-trending graben.

According to Yılmaz *et al.* (2000) and Akay and Erdoğan (2004), the N-S- and NE-SW-trending grabens were formed initially under an E-W-trending extensional regime during the Early Miocene. The extensional fractures associated with approximately N-S-trending oblique slip faults provided conduits for calc-alkaline, hybrid magmas to reach the surface (Yılmaz *et al.* 2000). A N-S extensional regime developed subsequently during the Late Miocene. During this time a major breakaway fault was formed; part of the lower plate was uplifted and later exposed in the Bozdağ Horst, and above the upper plate approximately N-S-trending cross-graben were developed. Alkaline basalt lavas were extruded along these fault systems (Yılmaz *et al.* 2000).

Erkül *et al.* (2004, 2005a, 2005b) carried out regional scale investigations of volcanism and structural features in the Bigadiç-Sındırgı region. The Kızıltepe Au-Ag deposit occurs approximately at the southeastern edge of the NE-SW-trending suite of subaerial volcano-plutonic rocks in the Sındırgı district. To the south, these mineralization-hosting units are partially constrained by the major north-dipping and listric (Seyitoğlu 1997) Simav graben-bounding fault (Figures 1 and 2).

The oldest units in the Sındırgı district are Paleozoic metamorphic rocks consisting of low-grade muscovite, chlorite, and quartz schists, and Late Cretaceous ophiolites. Magmatic activity in the area began with the Early Miocene Alaçamdağ granite (K/Ar: 19.9-27.9 Ma by Bingöl *et al.* 1982; U-Pb (zircon) ages: 20.0 ± 1.4 Ma and 20.3 ± 3.3 Ma, Rb-Sr (biotite) ages: 20.01 ± 0.20 Ma and 20.17 ± 0.20 Ma by Hasözbek *et al.* 2010), which cuts the metamorphic and ophiolitic basement rocks (Figure 2). The granitoid emplacement was followed initially by Early Miocene andesitic volcaniclastic lava and pyroclastic rocks (K/Ar: 23 ± 2.8 Ma, Erkül *et al.* 2005b). These volcanic rocks are overlain, in ascending order, by Early Miocene lacustrine sedimentary rocks, successive dacitic-rhyolitic rocks (K/Ar: 20.2 ± 0.5 Ma), rhyolitic lava flows, pyroclastic rocks (K/Ar: 20.5 ± 0.1 Ma), trachyandesitic intrusions (K/Ar: 20.6 ± 0.7 Ma), basaltic andesite intrusions (K/Ar: 17.8 ± 0.4 Ma), and associated lava flows and autobreccias (Erkül *et al.* 2005b). Erkül *et al.* (2005a) reported that two fault sets occur in the Sındırgı area; these are N0°-50°E-trending and 60°-90° NW-dipping oblique-slip and strike-slip faults, which are characterized by up to 100-m-wide shear zones contemporaneous with volcanism and sedimentation, and NW-trending faults dipping NE at angles of 55°-88° and showing right- and left-lateral oblique normal faulting.

3.2. Local geology

The Kızıltepe Au-Ag deposit and surrounding prospects are underlain by Cretaceous ophiolitic rocks (Figure 2) and limestone, which are overlain by a thick series of dacitic to rhyolitic lava domes (K/Ar: 20.2 ± 0.5 Ma; Erkül *et al.* 2005a), lava-flow breccias, and ignimbrites.

The ignimbrites preserved at the Kızıltepe deposit are subdivided into lower ignimbrite and upper ignimbrite units (Figure 3). The crystal-rich lower ignimbrite extends from Yusufçam village to the hot springs at Hisaralan along the Sındırgı-Simav road. The ignimbrite comprises quartz, K-feldspar, plagioclase, biotite, rare amphibole, crystal fragments, rock fragments, and minor pumice fragments, which are cemented by fine ash and, in places, recrystallized matrix. The average composition is 20%-40% quartz, 20%-40% K-feldspar (orthoclase ≈ sanidine), 0%-15% plagioclase, 0%-15% biotite, 0%-5% amphibole, 0%-5% rock fragments, 0%-5% pumice, and 10%-30% fine ash matrix. Higher in the lower ignimbrite unit, the crystal-rich ignimbrite passes gradationally into a brecciated ignimbrite subunit, which crops out in places to the north of the Sındırgı-Simav road (Figure 3), also suggesting some lateral gradation in this direction. The brecciated ignimbrite is characterized by medium- to coarse-grained, red to gray angular clasts set within a matrix of lower ignimbrite composition. The breccias appear to be derived from the underlying crystal-rich ignimbrite and are, therefore, classified as autoclastic breccia. The thickness of the lower ignimbrite unit is 250-300 m in the Kızıltepe area. $^{40}Ar/^{39}Ar$ dating of a groundmass separate of fresh sample taken from the lower ignimbrite unit 2 km NE of the Kızıltepe gold deposit (this study; see below) returned a plateau age of 19.82 ± 0.14 Ma.

The brecciated ignimbrite subunit is overlain by the upper ignimbrite unit, which consists of white to yellow pumice-rich pyroclastic flow deposits and crops out to

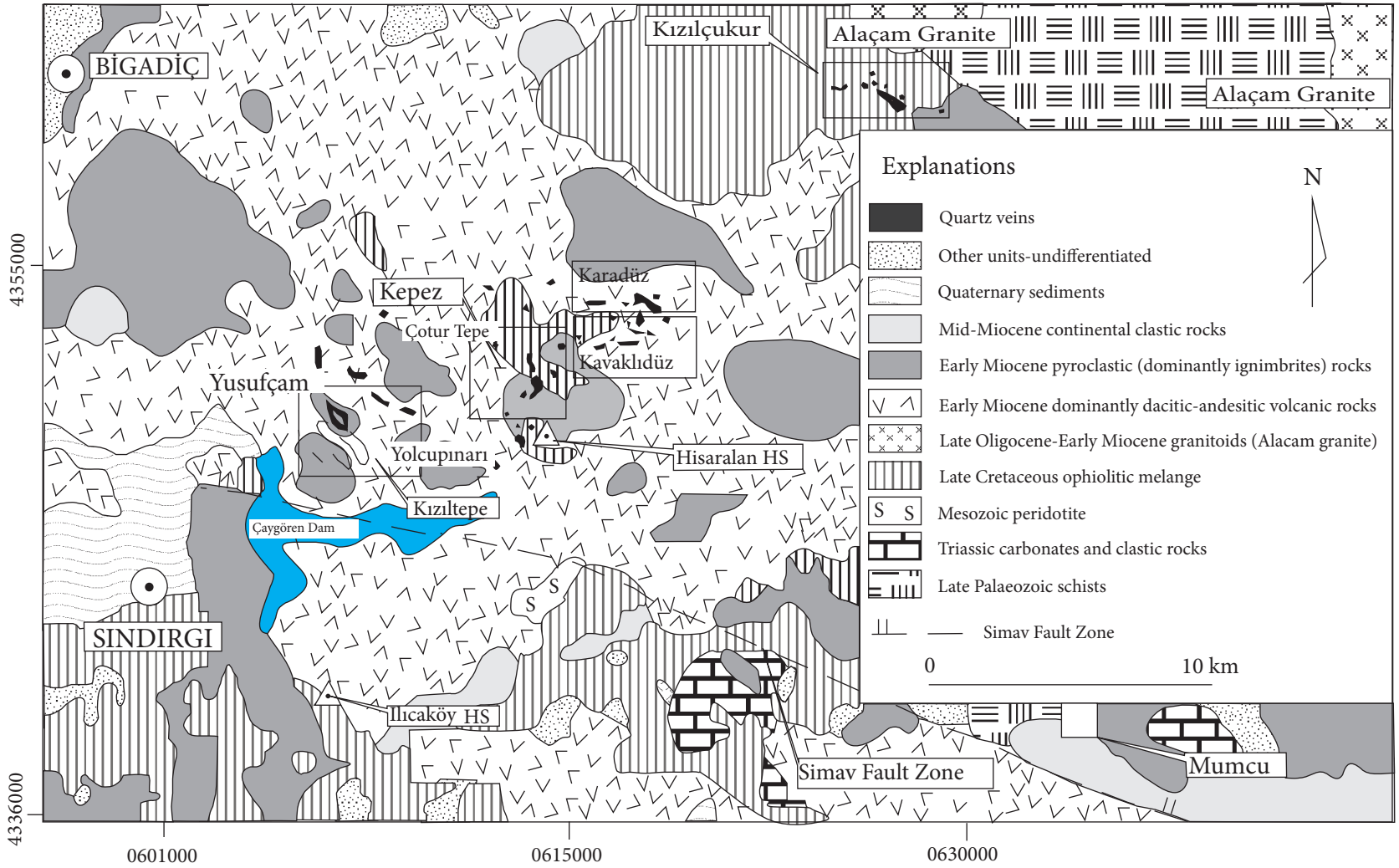

Figure 2. Regional geologic map of the Sındırgı area and the location of the Kızıltepe gold deposit and prospects (modified from Erkül 2005b and Şener *et al.* 2006).

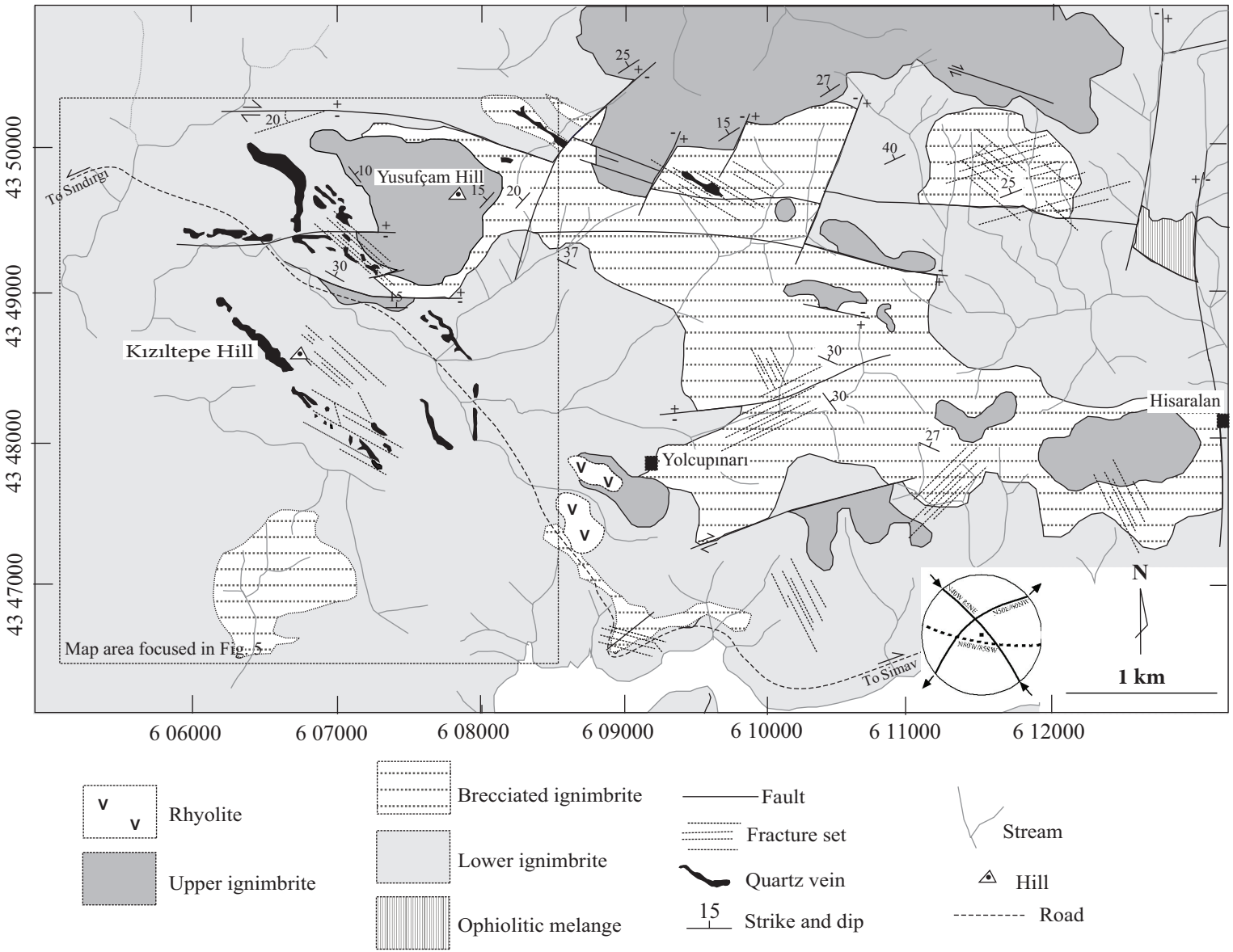

Figure 3. Geologic map of the Kızıltepe area. Stereographic projection shows the setting of the main E-W-trending faults and accompanying fracture sets mapped in the area. Dotted line represents E-W-trending faults and arrows show main stress orientations. Fractures are plotted from approximately 60 strike and dip measurements.

the north of the Kızıltepe deposit (Figure 3). The upper ignimbrite unit is characterized by a coarse-grained polymictic basal part, composed of lapilli to bomb-sized fragments derived from the lower ignimbrite unit, and pre-Tertiary basement rocks with pumice in a crystal fragment-rich ash matrix. The coarse-grained basal part grades upward into well-bedded and locally cross-bedded finer-grained, pumice-rich ignimbrites consisting predominantly of pumice fragments, glass shards, and crystal fragments in ash matrix. Grain composition consists of 50% pumice fragments, 15%-25% crystal fragments (quartz, K-feldspar, plagioclase, biotite), and 15%-25% glass shards. The upper ignimbrite unit is about 200 m thick in the Kızıltepe area.

The pyroclastic sequence in and around the Kızıltepe deposit is cut by white to yellow rhyolitic stocks exposed south of Yolcupınarı village (Figure 3). These massive, coherent rhyolitic lavas have significant steeply dipping flow foliation along their contacts and are surrounded by an autobrecciated periphery. The subvolcanic rhyolites are characterized by euhedral to subhedral phenocrysts in a glassy matrix; recrystallization or devitrification of the glassy matrix is a common textural characteristic. The mineral composition of the rhyolite is 30% quartz, 15% orthoclase, 10% sanidine, 20% plagioclase, 15% biotite, and 10% amphibole.

The basement rocks and ignimbrite sequence in the Kızıltepe area are cut by two sets of faults trending approximately E-W and NNE-SSW (Figure 3). In most locations, fault planes are typically not distinct enough to determine their displacement, and so the kinematic history of these faults is primarily inferred from stratigraphic relationships, alteration zonation, or a few slickensides. A major E-W-trending fault north of the study area (Figure 3) has argillic alteration at its western end and propylitic alteration at its eastern end. This fault plane shows slickensides with a rake of 20° and indicates dextral strike-slip displacement; the less prominent dip-slip component caused approximately 120 m of vertical displacement (Figure 3). In the pyroclastic sequence, parallel or subparallel synthetic and antithetic faults of this main E-W fault cause a southwards increase in preservation in the southern parts of the ignimbrite sequence. These synthetic faults are located at Yusufçam Hill along the Sındırgı-Simav road and near Yolcupınarı village, and are in places distinguished by moderate to strong argillic alteration developed along strike. The cumulative vertical displacement of these E-W dextral oblique-slip faults is about 250 m at the Kızıltepe deposit. The second significant fault set in the area trends N-S and cuts both the pyroclastic sequence and the E-W-trending faults. A significant N-S-trending fault is located at the eastern end of the area and bounds the Kızıltepe deposit. Parallel to subparallel minor synthetic and antithetic faults also occur in the area (Figure 3). From Kızıltepe Hill in the west (Figure 3) to Kepez Hill in the east, the deeper parts of the volcanic sequence are exhumed along these NNE-SSW faults. Around Hisaralan village (Figure 3) and further east, the basement ophiolites crop out. This stratigraphy indicates that vertical displacement was significant along the NNE-SSW faults, causing the exhumation of basement units. Thus, although no clear fault surface is preserved along this major NNE-SSW-trending fault system to define its kinematics, a dip–slip-dominated nature may be inferred from stratigraphic relationships.

NW-SE-trending fracture arrays cut the E-W faults at an angle of 30°-50° (Figure 3). This fracture set is extensional in nature, with 70°-90° dip angles, and hosts 0.1- to 1-m-thick quartz and calcite veinlets or veins. Economically significant gold-bearing quartz veins of the Kızıltepe deposit appear to be related to some of these NW-SE fractures. A second fracture set (NNE-SSW), which is compressional in nature, is almost perpendicular to the former extensional set and predictably does not contain any quartz or calcite fillings.

4. Hydrothermal alteration

Fine-grained pervasive silicification (Stage I silicification) is present in both the hanging-wall and foot-wall of the veins at Kızıltepe, particularly at the Arzu vein (Figure 4) where it is associated with coarse- to fine-grained quartz veins, veinlets, and stockwork. The silicified zones, which are cut by the quartz veins, veinlets, and stockwork, are, in turn, enveloped by argillic alteration (Figure 4). Within this envelope the original rock texture is largely preserved. Propylitic alteration, consisting mainly of pyrite and chlorite with minor smectite, occurs in the outer zone. The zone immediately adjacent to the quartz veins at Kızıltepe is dominated by quartz + adularia (minor) + illite, whereas smectite with minor mixed-layer illite/smectite occurs distal to the quartz veins (Appendix 1). Kandite-group (kaolinite) minerals occur throughout the Kızıltepe deposit. Alteration minerals at the Kepez and Kavaklıdüz prospects include quartz + adularia (minor) + illite + chlorite (Appendix 1).

Adularia occurs as massive replacement of metasomatized dacitic andesitic volcanic rocks, or as euhedral crystals growing within fractures in the Sındırgı area. Adularia is, in places, altered to clay within the veins at Kızıltepe and the related prospect veins. In summary, quartz-adularia-carbonate (carbonate is pseudomorphously replaced by quartz) veins with clay halos (illite, smectite) commonly host the Au-Ag mineralization.

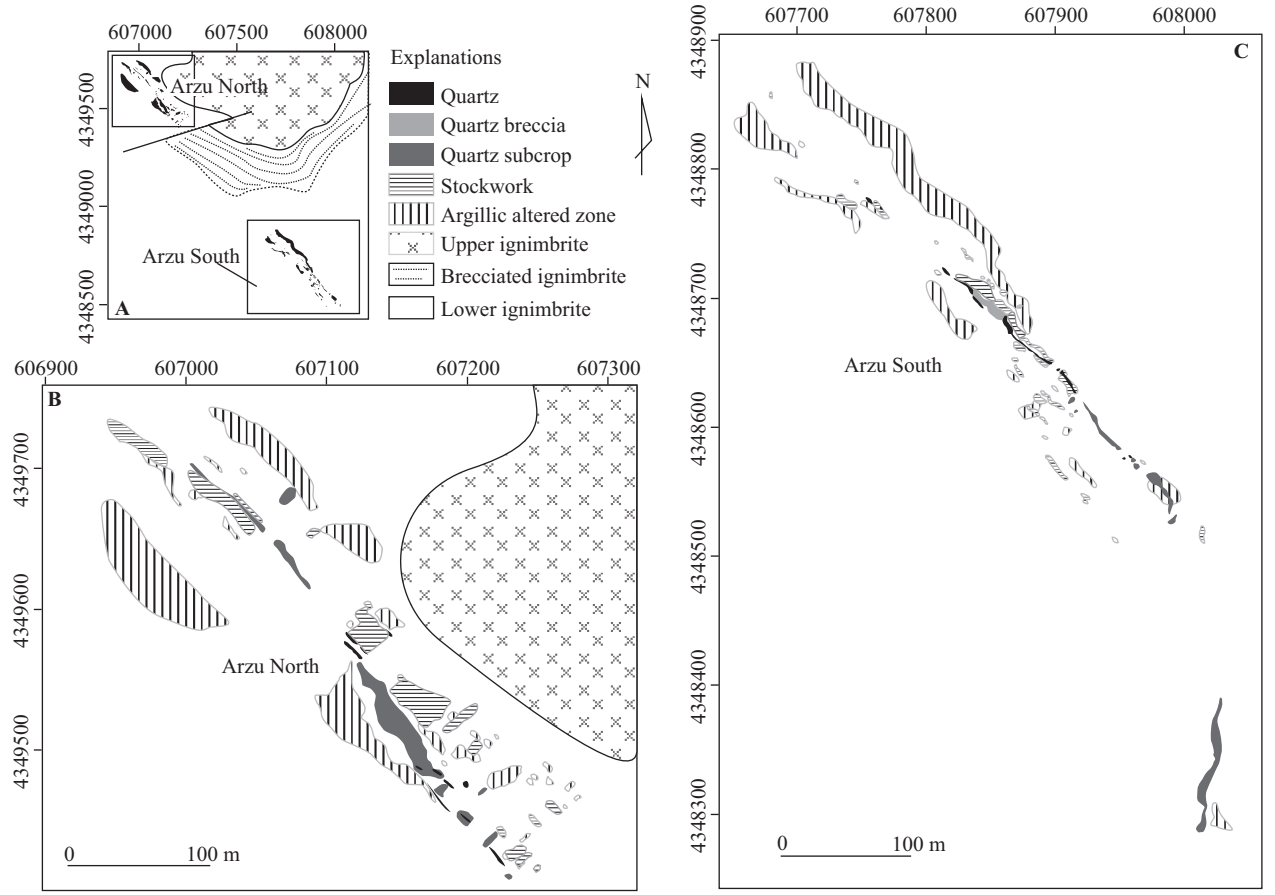

Figure 4. Alteration map of the Arzu vein (Kızıltepe gold deposit). Main map of the Arzu vein (A). Detailed alteration and mineralization map of Arzu North (B) and Arzu South (C) (modified from Şener *et al.* 2006 and this study).

5. Characteristics of the vein system

5.1. Kızıltepe gold-silver deposit

The Kızıltepe Au-Ag deposit consists of several typically NW-trending subparallel quartz veins and related stockworks (Figures 4 and 5), with a combined length of 19.5 km (Şener *et al.* 2006); the veins are hosted by crystal-rich, dacitic ignimbrite (the lower ignimbrite) near the village of Yusufçam. Four major lens-shaped veins and stockwork form the presently economic part of the deposit, referred to as the Arzu South, Arzu North, Banu, and Derya veins, which display similar morphology but show somewhat different textural characteristics. Only the Arzu South and Banu veins are discussed further here. The Arzu South vein has a mapped strike length of 950 m and an average 6 m of width (reaching a maximum of 14 m), and it ranges in dip from 70° to 85° NE, with a down-dip extension of >150 m (Figure 5); the Banu vein has a strike length of 800 m, averages 3 m wide (reaching a maximum of 6 m), and ranges in dip from 75° to 85° NW. The Banu vein exhibits evidence for shallow emplacement and low-temperature formation, as evidenced by ribbon-like features and common colloform/crustiform textures, particularly in the northwestern parts of the vein; this suggests that the distance from paleo-surface may be greater towards the southeast. Other veins close to the Banu veins also display shallow characteristics, indicated by low-temperature chalcedony and open-space quartz filling.

The margins of the veins have transitional lateral boundaries from a central body of quartz through to stockwork and then alteration; however, the gold grades decrease sharply from the vein into the wall rock. The Arzu South vein has an average grade of 6.28 g/t Au over 11 m, whereas the Banu vein has an average grade of 2.6 g/t Au over 2 m.

The Arzu vein contains four main textural types of mineralization: (a) crustiform (Cr) banded ore (typically 12 g/t Au and 190 g/t Ag), occurring as distinct bands of carbonate (Figure 6A) replacement and quartz; (b) bladed carbonate (Figure 6B); (c) matrix- to clast-supported fluidized (milled) breccia with subrounded to rounded clasts of vein quartz (Figure 6C), in which the massive

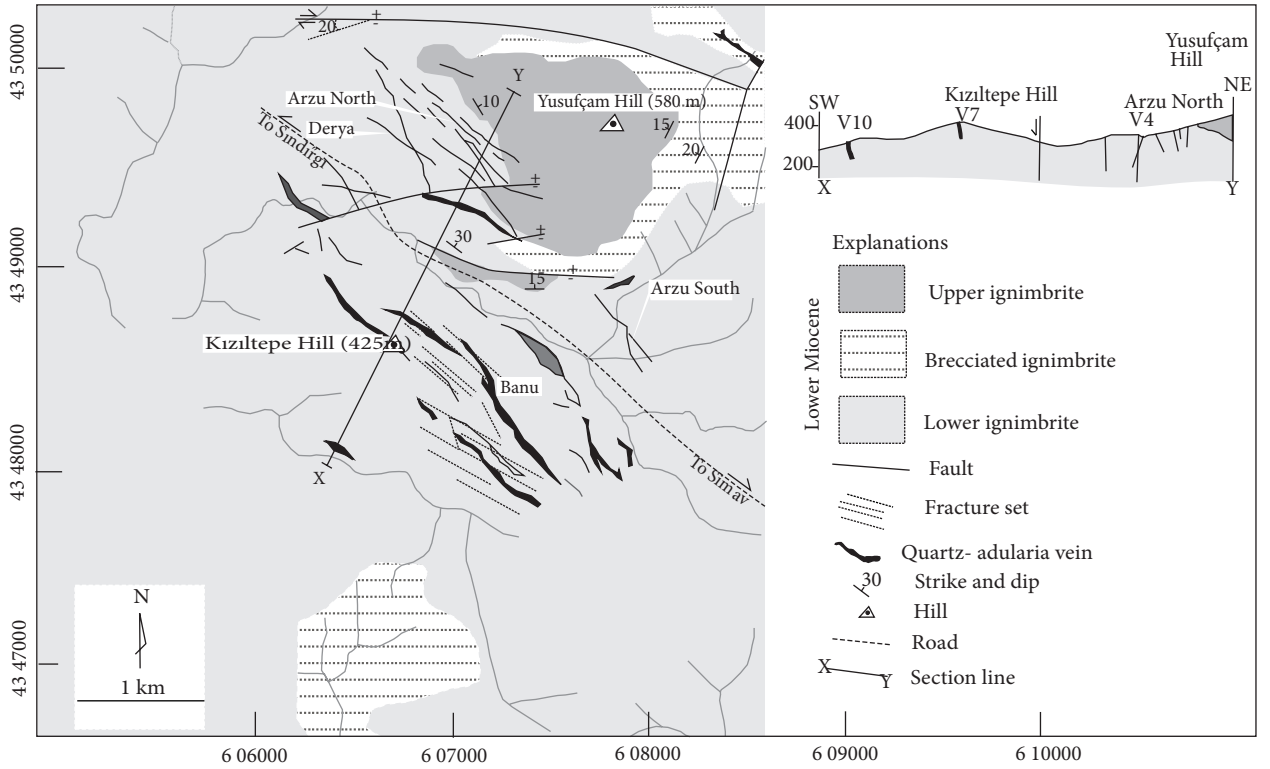

Figure 5. Geological map and cross-section of the Kızıltepe gold deposit.

clasts consist mainly of quartz and minor adularia; and (d) cockade texture formed from clasts of silicified wall rock or hydrothermally brecciated quartz vein material overgrown by crustiform/colloform bands and cockades of chalcedony quartz and adularia (Figure 6D).

5.2. The prospects

The Kepez prospect comprises 2.5 km of outcropping quartz veins, dominantly N-trending and bifurcating, which occur as a series of ridges near the village of Kepez (Figures 2 and 7). A large, 600-m-long N-S-trending vein up to 20 m wide at Karakaya Hill is located at the contact between dacite and ophiolitic rocks and dips 50° to the west. High-grade gold mineralization in this vein occurs in a matrix-supported hydrothermal breccia, which occurs over approximately 100 m of strike; drill hole data from this hydrothermal breccia suggest potential in this zone for 0.1 Mt at 6.7 g/t Au (Şener *et al.* 2006). Despite lower gold grades recorded from the surface of the Kepez prospect during initial exploration, evidence of extensive mine workings has been surprisingly encouraging to continue further work on the Karakaya vein by surface rock chip and rock-saw sampling. The surface sampling returned an average of 3.34 g/t Au, reaching a peak of 23.5 g/t Au, and 26.4 g/t Ag, reaching 99 g/t Ag. In the central part of the Kepez prospect area, the density of veins increases, as expressed by several N-S-trending ridges. The main prospect area at Kepez Tepe comprises a 5-m-wide silicified structure trending NE-SW over a 600 m strike length (Şener *et al.* 2006). Mineralized quartz veins host three textural types: (a) massive quartz (Figure 8A), (b) bladed carbonates (Figure 8B) occurring as bands of carbonate replacement, and (c) late-stage crackle quartz breccia (CBX) with limonitized (L) pyrite (Figure 8C).

The Karadüz prospect is located 4 km northeast of the village of Kepez (Figures 2 and 9). The area is part of a much larger system of alteration and vein development linked with the Kavaklıdüz prospect (Figures 2 and 9). Approximately 4 km total length of epithermal quartz veins and a large NW-SE-trending silicified ridge (200 m × 500 m) containing quartz veinlets and stringers are hosted mainly by volcaniclastic rocks and minor ignimbrite (unpublished company report, Galata Madencilik San. & Tic. Ltd. 2006). Along the ridge, there are old workings at the intersection of two distinct veins. Gold mineralization (up to 2.5 g/t Au) is hosted within quartz stringers in a foot-wall zone of massive silicification. Minor mineralization is also hosted by the contact zone between andesite lava flows and ophiolites in the western part of the prospect area. The veins at Karadüz contain several textural types: (a) colloform/crustiform (Col/Crs) banded texture (Figure 10A), which occurs both in the veins and as breccia clasts; (b) crudely banded (CrB) with

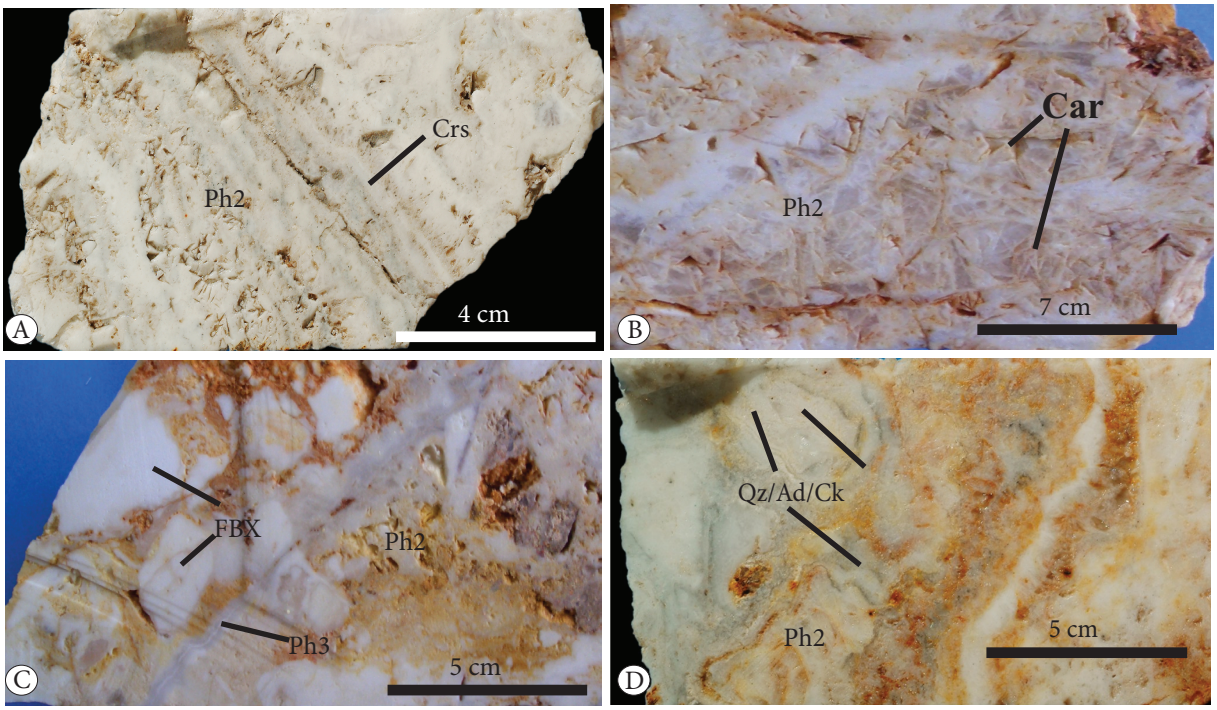

Figure 6. Macroscopic primary epithermal quartz vein textures from the Kızıltepe area: A) Crustiform (Crs) banded ore (12 g/t Au and 190 g/Ag), occurring as distinct bands of carbonate replacement. B) Coarse-banded chalcedonic quartz vein with bladed carbonate (Car) textures replaced by quartz. C) Matrix- to clast-supported fluidized (milled) breccia (FBX) with subrounded to rounded monomictic fragments representing the main mineralization phase (Ph1), in which the massive clasts consist mainly of quartz and minor adularia. Phase 1 is cut by chalcedony quartz veinlets (Ph2) with colloform banding. D) Cockade texture; formed from clasts of silicified wall rock overgrown by crustiform/colloform bands and cockades of chalcedonic quartz and adularia (11.9 g/t Au and 118 g/t Ag).

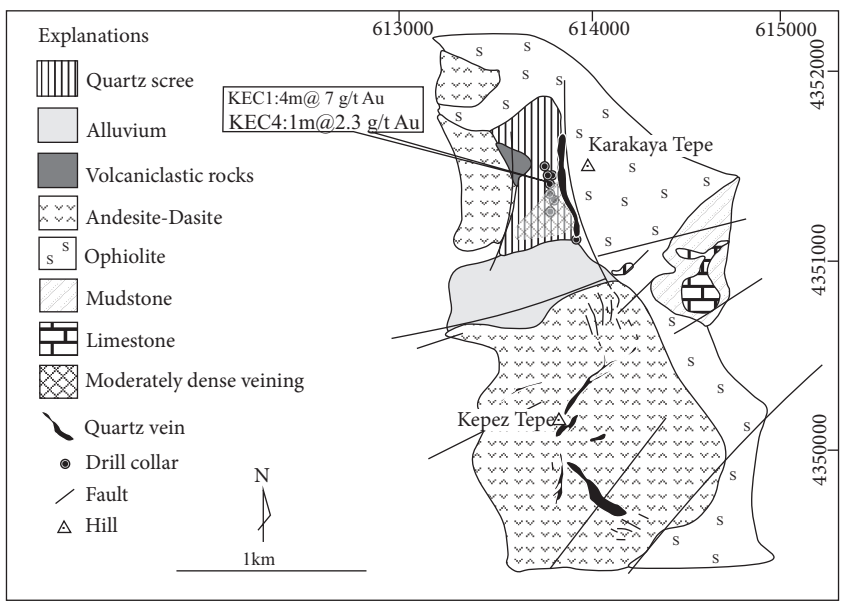

Figure 7. Geological map of the Kepez prospect (unpublished report by Şener *et al.* 2008).

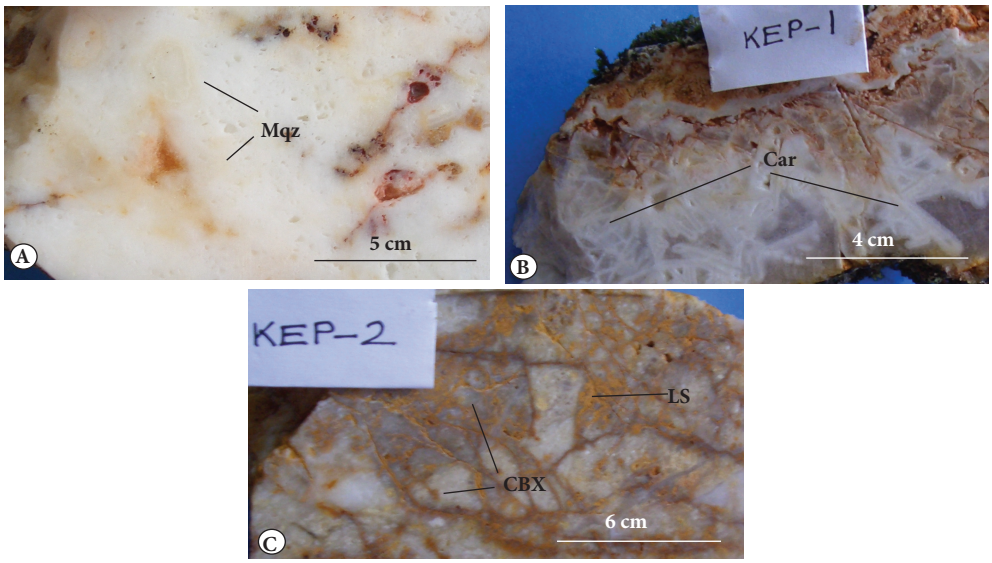

Figure 8. Macroscopic primary epithermal quartz vein textures from the Kepez area: A) Massive-textured quartz (Mqz) vein. B) Coarse-banded chalcedonic quartz vein with lattice-bladed carbonate (Car) textures replaced by: C) Late-stage crackle quartz breccia (CBX) with limonitized (LS) sulfide.

late-stage pyrite (Figure 10B); (c) crustiform (Crs), crudely banded, and mold-textured quartz veins (Figure 10C); (d) lattice-bladed carbonate replacement (Figure 10D); (e) matrix- to clast-supported hydrothermal breccia (VBX) with rounded clasts of vein quartz (Figure 10E); and (f) silicified porphyritic dacite (SiD) with colloform banded (Col) veinlets (Figure 10F).

The Kavaklıdüz prospect is located 3.5 km northwest of the village of Kepez (Figures 2 and 9) and comprises approximately 3 km total length of outcropping WNW- and ESE-trending epithermal quartz veins. The veins are hosted by crystal-rich ignimbrite (lower ignimbrite), undifferentiated volcaniclastic rocks, and andesite lava flow, which are cut by N- to NE-trending faults. Rock chip sampling of quartz from the veins returned several anomalous values of up to 3.5 g/t Au. Northwest of Kavaklıdüz, two areas of silicification returned values up to 2.6 g/t Au and 14.1 g/t Ag. Veins at the Kavaklıdüz prospect do not exhibit much textural variation; massive quartz (as at Kepez, Figure 8A) and lattice-bladed carbonate (LBCar) replacement (Figure 11) textures are dominant.

6. Vein mineralogy of the Kızıltepe gold deposit and prospects

6.1. Gangue mineralogy

The quartz veins in the Kızıltepe deposit consist mainly of fine- to coarse-grained (Figure 12A) quartz (Qz) with minor adularia (Ad) and chalcedony (Figure 12B). Evidence of at least two episodes of quartz deposition (Figures 12A-12C) is present, as well as the formation of quartz after earlier calcite. Calcite also occurs as bands or fills vugs in the quartz veins, and in places it comprises a network of lattice blades (L.Ca; Figure 12D) separated by polyhedral cavities or fan-shaped blades (FB) already replaced by quartz (Figure 12E). Similar lattice quartz probably originated as pseudomorphs after bladed calcite (Simmons & Christenson 1994). Adularia occurs as euhedral rhombs within fissure veins cutting altered dacitic volcanic rocks (Figure 12C). Micro-plumose (MP) textures are common, displaying a feathery appearance in domains within quartz crystals related to the formation of crystallites during recrystallization of chalcedony (Figure 12F). In addition to these textures, original quartz vein clasts are in places overgrown by chalcedonic colloform bands (Figure 12G).

The highest gold grades, ranging from 12 to 32.5 ppm in the Kızıltepe veins, are associated with crustiform quartz-adularia; quartz-adularia vein breccia with colloform, crustiform, cockade, and carbonate replacement textures; and quartz vein breccia with quartz matrix, whereas massive chalcedony contains less to negligible gold (<0.5 ppm). In addition, some parts of the quartz veins with very well-developed colloform/crustiform banding contain negligible gold, e.g., at the Karadüz prospect (Figure 10A).

6.2. Ore mineralogy

The Kızıltepe deposit has simple ore mineralogy, consisting mainly of disseminated pyrite and Fe-oxide (related to oxidation of pyrite) with traces of electrum, acanthite, Au-rich acanthite, and Ag-Hg-Au-Tl-Te-Pb compounds (with

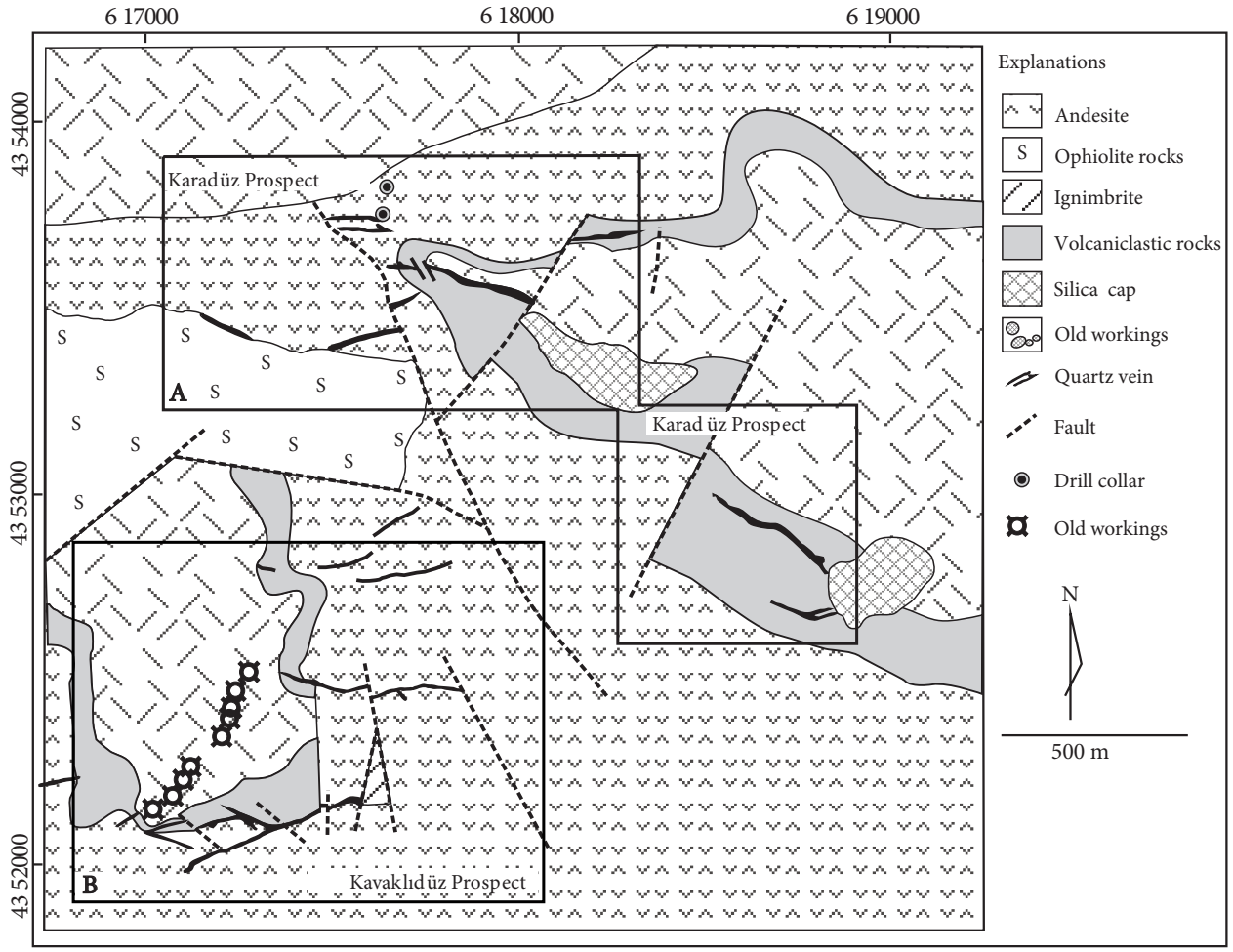

Figure 9. Geologic map of the A) Karadüz and B) Kavaklıdüz prospects (unpublished report by Şener *et al.* 2008).

Ag > 80%). In general, the ore minerals occur mostly as disseminations within veins and subordinate stockwork veinlets. Ore mineral assemblages identified at Kızıltepe are typical of low-sulfidation epithermal systems (e.g., Hedenquist *et al.* 2000; Simmons *et al.* 2005).

Gold occurs as fine (<0.03 mm) grains (Figure 13A) of electrum (average composition of 53% Au, 41% Ag with associated 2.5% Pb and 1.5% Bi; Table 1), or as discrete native grains, precipitated between the interstices of quartz crystals (Figures 13B and 13C), and is accompanied by acanthite (average composition of 77% Ag, 3.7% Au, 2.1% Pb, 1.5% Hg, and 1.3% Tl); gold is often in sharp contact with acanthite (Figures 13D and 13E, Table 1). Electrum- and gold-rich acanthite (average composition of 72.2% Ag, 6.5% Au, 3.2% Sb, 2.5% Bi, 1.8% Pb, and 1% Hg) form a diffuse contact with sulfur-free (Ag-Hg-Au-Tl-Te-Pb) compounds (average composition of 80% Ag, 3.8% Au, 4.7% Hg, 3.2% Tl, 3.1% Te, and 2.7% Pb; Table 1, Figure 13F). Acanthite occurs both in discrete grains (Figure 13G) and as cluster-filling interstices in quartz gangue.

Based on microstructural evidence, the vein mineralization is subdivided into three main stages; these are pre-ore-, ore-, and supergene or post-ore-stages (Figure 14). The pre-ore stage, which predates gold mineralization, consists mainly of microcrystalline barren quartz, pyrite, and chlorite, and minor smectite and mixed-layered illite/smectite. The fluids of the first stage may be partly responsible for the silicification and argillic alteration of the host rocks. The Kızıltepe Au-Ag ore veins show evidence for three periods of hypogene mineralization, separated by phases of fracturing and brecciation. Of these, the first mineralization phase (Phase I, Figure 14) is characterized by deposition of coarse-grained quartz (Figure 12A: Cqz 2), illite, pyrite, and minor precious metals. The second mineralization phase (Phase II, Figure 14) is represented by the major gold-bearing quartz veins, which commonly exhibit crustiform banding, carbonate replacement, and hydrothermal breccia textures (Figures 12B-12G). The third and minor mineralization phase (Phase III, Figure 14) is represented by narrow chalcedony

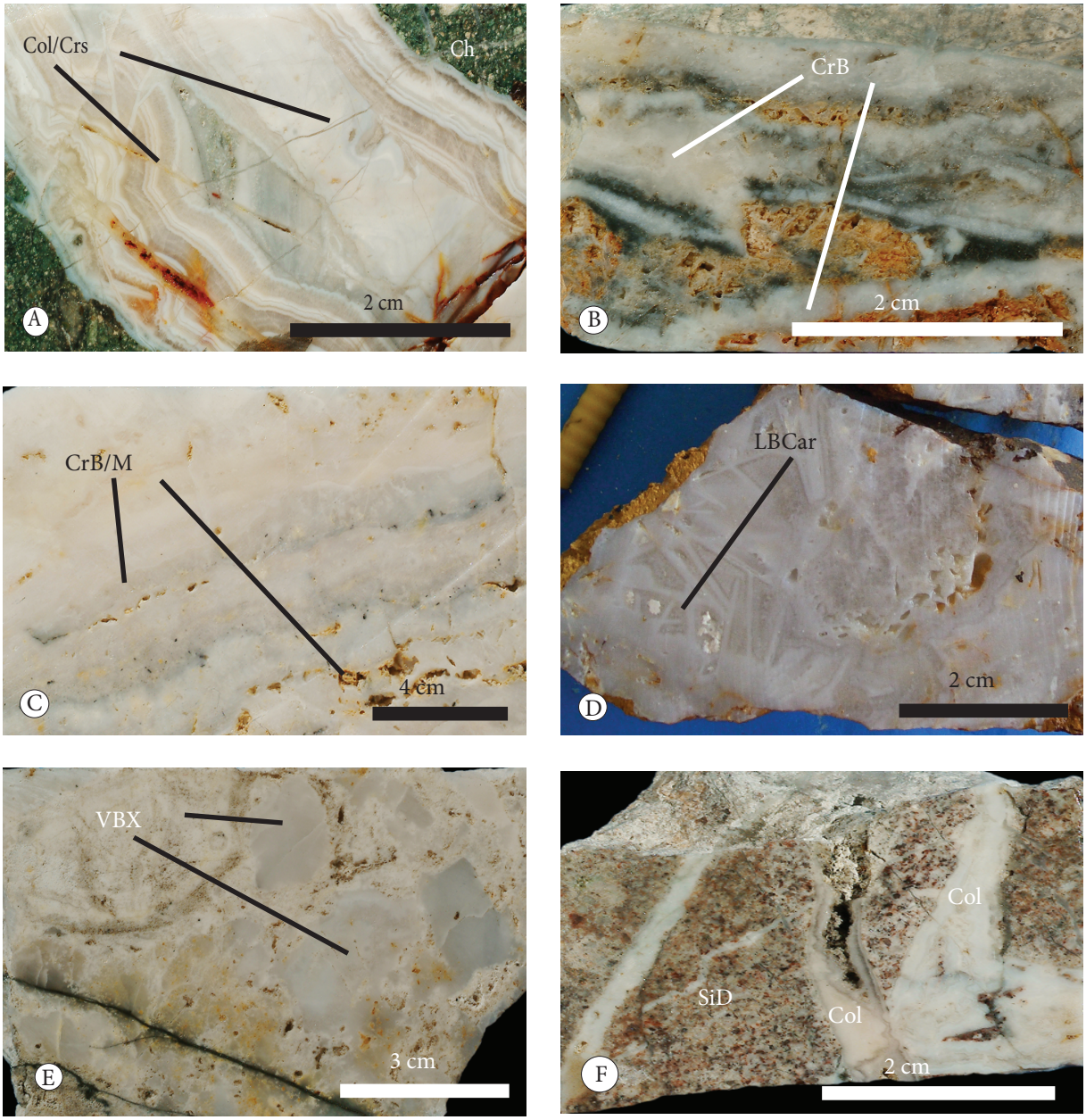

Figure 10. Macroscopic primary epithermal quartz vein textures from the Karadüz area: A) Colloform/crustiform (Col/Crs) banded quartz vein (Au: 0.08 g/t and Ag: 2.53 g/t Ag), which occurs in both the veins and as breccia clasts. B) Crudely banded (CrB) vein quartz (Au: 0.31 g/t and Ag: 1.28 g/t Ag) with late-stage pyrite. C) Crustiform (Crs), crudely banded, and molded quartz (CrB/M) vein (Au: 1.6 g/t and Ag: 108 g/t Ag). D) Lattice-bladed carbonate (LBCar) replacement texture. E) Matrix- to clast-supported hydrothermal breccia (VBX) with rounded monomictic fragments, in which the massive clasts consist mainly of quartz. F) Silicified porphyritic andesite (SiAn) with colloform banded (Col) veinlets (Au: 0.17 g/t and Ag: 0.66 g/t Ag).

quartz vein/veinlets with colloform banding, which cuts the earlier phases (Figures 12A and 12C). Lastly, the post-ore supergene mineral assemblage consists of native gold, Fe-oxides (goethite) with a colloform banding texture (Figure 13H), and supergene kaolinite.

7. Analytical methods and procedures

Clay identification for unoriented and oriented samples was accomplished using a Philips X-ray diffractometer, which utilizes a nickel filter with CuKα radiation at 40 kV and 20 mA (Appendix 2).

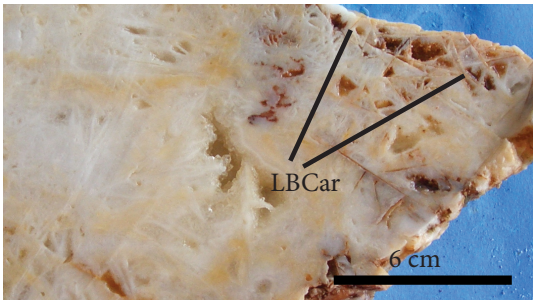

Figure 11. Lattice-bladed carbonate (LBCar) replacement and massive quartz (as in Kepez in Figure 8A) textures in the Kavaklıdüz area.

Adularia from quartz-adularia veins and groundmass separates from the ignimbrites were selected for $^{40}Ar/^{39}Ar$ geochronology in order to establish the temporal relationship between magmatism, deformation, and mineralization at Kızıltepe (Table 2). The $^{40}Ar/^{39}Ar$ technique was applied following the procedures of the University of Nevada, Las Vegas, outlined by Staudacher *et al.* (1978). Synthetic K-glass and optical grade CaF_2 were included in the irradiation packages to monitor neutron-induced argon interferences from K and Ca. Loaded tubes were packed in an Al container for irradiation and 200 mg samples were irradiated at McMaster Nuclear Reactor at McMaster University, Ontario, Canada (Appendix 2).

For geochemical analysis, 5 g of sample pulp were crushed to 100-mesh size and about 0.2 g was used for the ICP-MS determinations at ACME Laboratories, Canada. Fifteen elements were analyzed, including Mo, Cu, Pb, Zn, Ni, As, Cd, Sb, Bi, Ag, Au, Hg, Tl, Se, and Sc, following a $HCl-HNO_3-H_2O$ leaching at 95 °C (Table 3). For the remaining elements, including the major oxides (SiO_2, Al_2O_3, Fe_2O_3, MgO, CaO, Na_2O, P_2O_5, MnO) and the rare earth and incompatible elements, the $LiBO_2$ fusion preparation method was used prior to ICP-MS analysis (Appendix 2).

For microthermometric analysis, doubly polished thin sections, approximately 100 µm thick, were prepared from more than 15 drill core samples from depths of 30 to 100 m from the Arzu South vein and outcrop samples at the Kızıltepe deposit and the prospects. A total of 172 fluid inclusions were studied; homogenization temperatures (T_h), first melting temperatures (T_{mf}), and melting temperatures of ice (T_m) were measured (Appendix 2).

8. Geochronology

8.1. $^{40}Ar/^{39}Ar$ results

One sample (YN-5) from the Arzu South quartz-adularia vein in the Kızıltepe deposit yields both a plateau age (65% of the total ^{39}Ar released) of 18.27 ± 0.11 Ma and a total gas age of 18.14 ± 0.09 Ma. The initial two steps (approximately 20% of the ^{39}Ar released) and the final steps (approximately 10% of the ^{39}Ar released) are younger, with the exception of the second step (Table 2). Steps 3-6 (65% of the ^{39}Ar released) define a slightly older, but analytically indistinguishable, plateau age of 18.27 ± 0.11 Ma (Figure 15A). Steps 3-9 define a statistically valid isochron, which yields an age of 18.50 ± 0.05 Ma, and a $^{40}Ar/^{39}Ar$ intercept of 224 ± 3 (Figure 15B). The plateau age and the isochron age overlap at ±2σ analytical uncertainty. However, the $^{40}Ar/^{39}Ar$ intercept is anomalously low and, therefore, makes this isochron age suspect. Generally, fractionation of atmospheric argon has been shown to produce initial $^{40}Ar/^{39}Ar$ ratios of about 280-285 at the lowest. Ratios of 224, thus, must be considered spurious, and the isochron unreliable. The plateau age (18.27 ± 0.11 Ma) for this sample appears reliable as the plateau age is generally well behaved.

One sample from the upper ignimbrite (S-817) unit located 2 km NE of the Kızıltepe deposit produced a nearly ideal flat age spectrum, with only minor discordance. The total gas age is 19.03 ± 0.10 Ma. Steps 8-11 (78% of the ^{39}Ar released) define an analytically indistinguishable plateau age of 18.96 ± 0.11 Ma (Table 2, Figure 15C). The same steps define a statistically valid isochron, which yields an age of 19.05 ± 0.11 Ma, and a $^{40}Ar/^{39}Ar$ intercept of 287 ± 11 (Figure 15D). All these ages are indistinguishable at ±1σ analytical uncertainty, and thus it makes little difference as to which is used in that respect. However, the isochron is defined by only four data points, which are all nearly of the same radiogenic yield; thus, the data are highly clustered. For this reason, the plateau age for this sample is preferred. The isochron does not indicate that any excess argon is present and, therefore, the age spectrum should yield accurate ages.

A sample from the lower ignimbrite unit (S-756) located 1 km N of the Kızıltepe deposit produced an age spectrum that is nearly ideal and perfectly flat, with only minor discordance. The total gas age is 19.76 ± 0.12 Ma (Table 2). Steps 5-11 (52% of the ^{39}Ar released) define an indistinguishable plateau age of 19.82 ± 0.14 Ma (Figure 15E). Steps 4-9 define a statistically valid isochron, which yields a significantly older age of 20.91 ± 0.21 Ma, and an $^{40}Ar/^{36}Ar$ intercept of 282.4 ± 2.5 (Figure 15F). In this case, the isochron is defined by six points, which comprise <50% of the total gas released, somewhat clustered near the center of the isochron line. The isochron also yields an age that is about 1 Ma older than the total gas and plateau ages. For these reasons, this isochron age is considered less reliable than the plateau age, which is preferred and is considered a highly reliable age.

9. Geochemistry

Samples of unaltered, altered, and mineralized rocks in this study provide an opportunity to investigate variations

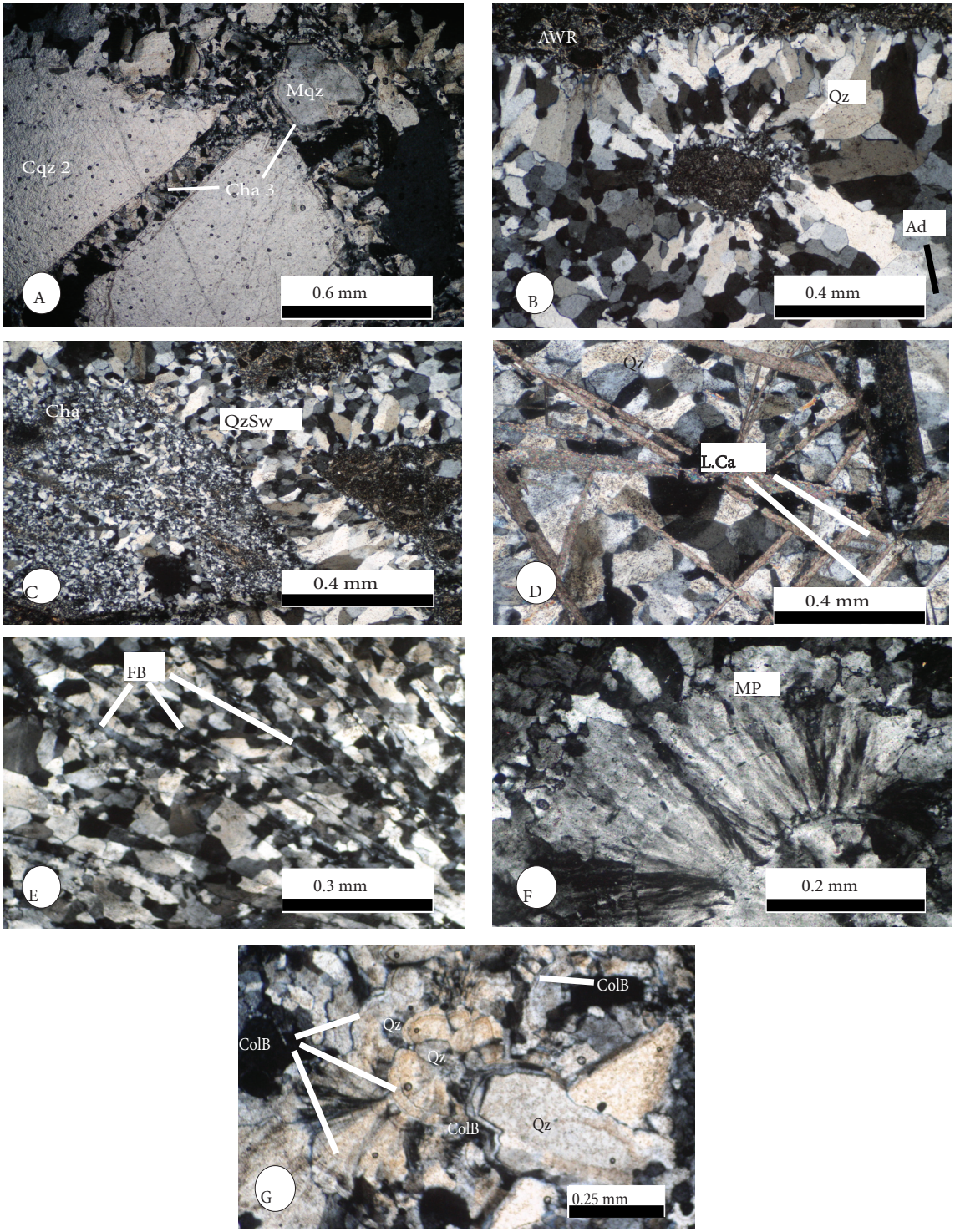

Figure 12. Photomicrographs (under crossed Nichols) of primary epithermal quartz textures: A) Coarse (Cqz: Phase I) and medium (Mqz: Phase II)- to fine (Cha)-grained quartz, chalcedony quartz (Phase III) cutting earlier coarse quartz or overgrowing medium quartz. B) Medium- to fine-grained quartz (Qz) with minor euhedral adularia (Ad) and chalcedony in the vein cutting altered wall rock (AWR). C) Argillitized and silicified (cha: chalcedony) dacitic ignimbrite wall rock is cut by stockwork crystalline quartz veinlets (QzSw). D) Calcite is present as a network of intersecting or lattice blades (L.Ca) separated by polyhedral quartz fields (Qz). E) Fan-shaped (FB), originally calcite blades replaced by quartz. F) Micro-plumose (MP) texture with feathery appearance within quartz crystals related to the formation of crystallites during recrystallization of chalcedony. G) Clasts of quartz (Qz) vein are overgrown by colloform bands (CoB).

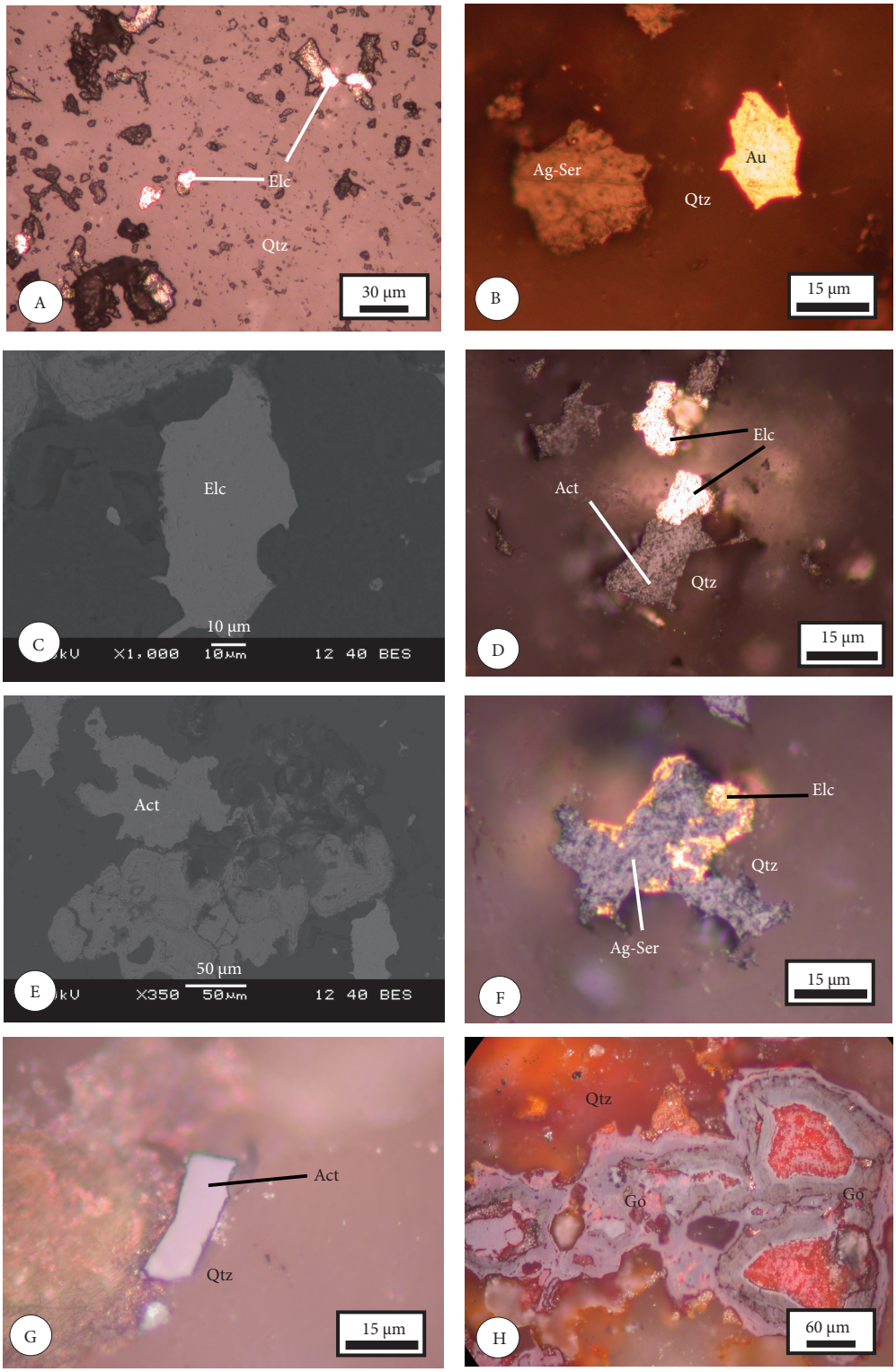

Figure 13. Ore mineralogy (reflected plane-polarized light (except G and H which are SEM-BSE images)): A) Gold occurs as fine (<0.06 mm) subhedral grains of electrum (Elc). B) Native Au filling a vug rimmed by euhedral quartz gangue minerals. C) SE-SEM image of gold occurring in discrete native grains, precipitated between the interstices of quartz gangue. D) Anhedral electrum (Elc) showing sharp contacts with acanthite (Act). E) SE-SEM image of an achantite cluster filling interstices in quartz gangue. F) Electrum (Elc) probably showing a diffuse contact with the Ag-Te-Hg-Au-Tl-Pb series (Ag-Ser). G) A discrete subhedral acanthite (Act) grain. H) Goethite with colloform texture filling interstices in quartz gangue.

Table 1. SEM analysis of gold and silver minerals in the Kızıltepe gold deposit.

Sample no.	550511	555228A	559120	Average*	555228A	555228A	559120	559120	559120	Average*	555228A	555228A	Average*	559120	550511	Average*
	No: 5.2	No: 3.1	No: 1. Edge2		No: 2.2	No: 2.3	No: 1. Edge1	No: 1 Middle2	No: 1 Middle3		No: 2.1	No: 3.2		No: 1 Middle1	No: 5.1	
Element	Electrum	Electrum	Electrum	Electrum	Acanthite	Acanthite	Acanthite	Acanthite	Acanthite	Acanthite	Au-rich Acanthite	Au-rich Acanthite	Au-rich Acanthite	Ag-Hg-Au-Tl-Pb compounds	Ag-Te-Hg-Au-Tl-Pb compounds	Ag-Te-Hg-Au-Tl-Pb compounds
S	0.09	0.00	0.00	0.00	10.70	11.58	9.27	13.02	10.15	10.94	11.14	10.81	10.98	0.00	0.00	0.00
Cu	–	–	0.35	0.12	–	–	0.29	0.27	0.36	0.18	–	–	–	0.33	0.40	0.37
Pb	2.65	2.65	2.24	2.51	2.83	2.55	2.08	1.33	1.86	2.13	1.60	1.98	1.79	2.65	2.67	2.66
Zn	0.34	0.34	0.31	0.33	0.23	0.21	0.55	0.26	0.38	0.33	0.40	0.17	0.29	0.33	0.28	0.31
As	0.00	0.00	0.00	0.00	0.4	0.32	0.00	0.21	0.00	0.19	0.14	1.79	0.97	0.00	0.28	0.14
Sb	0.00	0.00	0.00	0.00	3.84	4.98	0.00	0.00	0.00	1.76	4.25	2.21	3.23	0.00	1.38	0.69
Se	0.00	0.00	0.00	0.00	0.31	0.61	0.34	0.69	0.22	0.43	0.46	0.44	0.45	0.59	0.60	0.60
Ag	42.26	42.23	39.1	41.2	74.24	72.37	81.10	76.44	80.02	76.83	72.94	71.53	72.23	85.39	75.90	80.65
Au	51.7	51.73	55.5	52.98	3.64	4.28	3.68	3.78	3.05	3.69	5.39	7.61	6.50	3.64	3.92	3.78
Te	0.35	0.35	0.7	0.47	0.00	0.00	0.07	0.00	0.17	0.05	0.00	0.00	0.00	0.01	6.27	3.14
Hg	0.35	0.35	0.17	0.29	1.65	1.36	1.14	1.48	1.80	1.49	1.28	0.78	1.03	4.02	5.37	4.70
Tl	–	–	1.66	0.55	–	–	1.55	2.52	2.00	1.26	–	–	–	3.04	3.31	3.18
Mg	0.09	0.08	–	0.06	1.95	0.20	–	–	–	0.43	0.04	0.09	0.07	–	–	–
Bi	2.23	2.23	–	1.49	–	1.53	–	–	–	0.31	2.34	2.60	2.47	–	–	–
Total	100.06	99.96	100.03	100.02	100.00	99.99	100.07	100.00	99.99	100.02	100.00	100.01	100.01	100.00	100.40	100.22

Average*: Average of columns on the left.

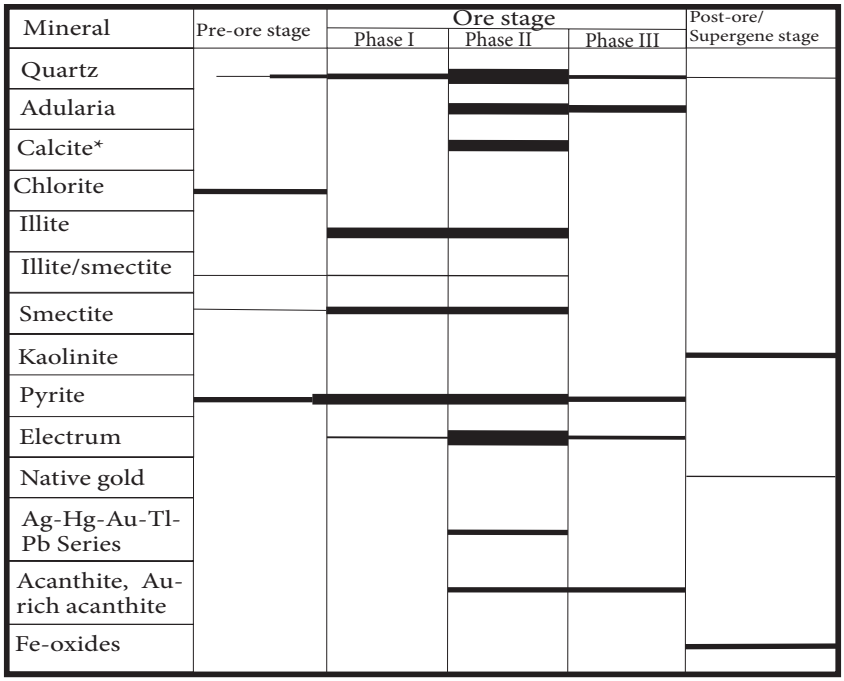

Figure 14. Generalized paragenetic scheme for the Kızıltepe gold-silver deposit. Line width indicates abundance (fine: scarce, thick: abundant).

in precious and base metals, REEs, minor elements, and major oxides in hydrothermally altered volcanic rocks that host quartz-adularia-type epithermal Au-Ag deposits (e.g., Palacios *et al.* 1986; Bierlein *et al.* 1999; Yılmaz *et al.* 2000; Bi *et al.* 2004). Data for all samples are presented in Appendix 3.

The degree of hydrothermal leaching of wall rock in the Kızıltepe deposit and the prospects is variable for major and trace elements. Cesium is enriched slightly whereas Ba, Th, U, Nb, and Ti show up to one- to two-fold depletions in altered wall rocks (Figure 16A). Of the trace elements, Zn shows the greatest decrease, with eight-fold depletion. Of the major elements, K and Ca display slight enrichments, while Na and Mg are depleted by factors of 23 and 9, respectively. Due to structurally controlled pervasive alteration, Na and Mg are depleted whereas K and Cs are enriched slightly, due to the formation of illite or adularia (Appendices 1 and 3, Figures 16A and 16B); Zn displays similar depletion patterns. All REEs in altered wall rock typically display a flat and depleted pattern, at ratios slightly less than unity (by a factor of about 2) relative to fresh rock, except Eu, which sits at the unity line (Figure 16). Trace elements such as Ba, Th, U, Nb, La, Ce, Sr, Nd, Zr, Ti, Tb, Y, and Cr are very low in mineralized quartz veins in the Kızıltepe deposit and the prospects (Figure 17). The average concentration of Mg, Fe, Na, and Ca (Figure 16A) is also extremely low (Appendix 3). All LREE (La-Eu) concentrations in quartz veins are significantly lower than those of the host volcanic rocks (Figure 16B). A progressive relative enrichment from La through Ce, Pr, Eu, Gd, Tb, Ho, and Tm to Lu is present, with decreasing depletion factors of 15 to 75 across these elements.

Figure 18 depicts chondrite-normalized REE profiles of fresh volcanic rocks, altered volcanic rocks, and quartz veins. All REE chondrite-normalized patterns within altered volcanic rocks and mineralized quartz veins in the Kızıltepe deposit and the prospects show some systematic decrease relative to the fresh volcanic rocks. Evidence for remobilization of REE at the Kızıltepe deposit and the prospects is provided by their consistent decrease from fresh volcanic rocks through mixed-layer illite/smectite and kaolinite-altered volcanic rock to quartz-adularia veins (Figure 18). However, LREE and HREE concentrations are noticeably lower in the quartz-adularia veins (Figures 17 and 18). Eu, Dy, Er, and Yb show weak negative anomalies, probably inherited from major element removal from the volcanic rocks (Bierlein *et al.* 1999). The general REE patterns of altered volcanic rock and adularia-quartz veins are almost identical to each other, probably indicating that there is no external fluid involvement through the alteration stages.

The average Rb/Sr ratios of unaltered fresh volcanic rocks, altered volcanic rocks, and quartz veins at the Kızıltepe deposit and the prospects are 0.34, 0.46, and

Table 2. Results of $^{40}Ar/^{39}Ar$ analysis of the Kızıltepe (Sındırgı) gold deposit and surrounding ignimbrites.

Step	T*	^{36}Ar	^{37}Ar	^{38}Ar	^{39}Ar	^{40}Ar	% ^{40}Ar	% ^{39}Ar rlsd	Ca/K	$^{40}Ar/^{39}ArK$	Age (Ma)
Lower ignimbrite-756 (Kızıltepe), groundmass separates: 34.80 mg, J = 0.001937 ± 0.39%											
1	650	54.89	65.077	16.611	500.351	18,756.44	15.2	18.413.535	0.6868038	5.709836	19.069
2	700	3.672	76.112	5.086	361.532	3210.9	67.5	13.304.824	1.111.838	5.990154	20.00
3	750	2.505	25.894	3.433	239.137	2147.11	67.0	8.800537	0.5717641	5.981721	19.972
4	800	2.386	14.295	2.55	166.115	1692.24	60.0	6.1132374	0.4543860	6.065452	20.25
5	850	3.495	15.819	2.765	158.839	1963.34	49.0	5.845471	0.5258730	6.0265973	20.121
6	910	5.877	18.004	3.999	211.036	2953.84	42.7	7.766385	0.450465	5.9621462	19.907
7	970	9.072	22.336	6.256	324.094	4522.35	42.1	11.9270599	0.3638918	5.8681938	19.595
8	1040	7.361	23.915	5.749	292.989	3865.17	45.1	10.7823574	0.4309885	5.942270	19.841
9	1110	4.328	19.223	3.328	137.97	2057.42	39.6	5.077466602	0.7357373	5.85434330	19.549
10	1180	8.325	21.603	5.087	189.241	3551.78	32.3	6.9643028	0.602792	6.045271	20.183
11	1250	4.752	16.426	2.628	92.003	1910.6	28.4	3.38582416	0.942851	5.836880	19.491
12	1400	2.33	20.323	1.484	43.989	939.404	29.5	1.6188495	2.440910	6.1413632	20.502
					Cumulative % ^{39}Ar rlsd =			100.0	Total gas age =		**19.76**
									Plateau age (steps 5-11) =		**19.82**
									Isochron age (steps 4-9) =		**20.91**
Step	T*	^{36}Ar	^{37}Ar	^{38}Ar	^{39}Ar	^{40}Ar	% ^{40}Ar	% ^{39}Ar rlsd	Ca/K	^{40}Ar ^{39}ArK	Age (Ma)
Upper ignimbrite-817 (Kızıltepe), groundmass separates: 34.80 mg, J = 0.00186 ± 0.42%											
1	600	5.761	0.343	1.957	66.722	2122.72	21.6	0.85071	0.0267364	6.736088	23.387
2	675	0.366	0.218	0.832	60.591	438.041	79.7	0.772544	0.0187122	5.522536	19.196
3	750	0.333	0.308	1.255	98.77	628.06	87.7	1.2593331	0.0162182	5.419003	18.838
4	810	0.646	0.462	1.955	147.118	982.334	82.7	1.875777	0.0163325	5.431438	18.881
5	880	0.824	0.72	3.191	250.319	1608.1	86.2	3.1916068	0.0149594	5.488987	19.08
6	970	1.539	1.308	5.924	458.08	2937.86	85.3	5.840592	0.0148505	5.453705	18.958
7	1060	3.276	1.794	8.597	649.932	4564.18	79.4	8.286735	0.0143559	5.573731	19.373
8	1130	2.894	2.308	10.642	824.525	5331.48	84.4	10.512824	0.0145582	5.456018	18.966
9	1200	5.099	4.877	22.213	1739.199	10,917.23	83.1	22.175062	0.0145841	5.434329	18.891
10	1290	9.785	7.301	33.2	2579.1	16,891.11	91.8	32.88393	0.0147228	5.456307	18.967
11	1400	1.684	2.766	12.151	968.679	5780.19	91.8	12.350810	0.01485078	5.472213	19.022
					Cumulative % ^{39}Ar rlsd =			100.00	Total gas age =		**19.03**
									Plateau age (steps 8-11) =		**18.96**
									Isochron age (steps 8-11) =		**19.05**
Step	**T***	**^{36}Ar**	**^{37}Ar**	**^{38}Ar**	**^{39}Ar**	**^{40}Ar**	**% ^{40}Ar**	**% ^{39}Ar rlsd**	**Ca/K**	**$^{40}Ar/^{39}ArK$**	**Age (Ma)**
YN-5 (Arzu vein vein/Kızıltepe Au deposit), adularia: 23.10 mg, J = 0.001956 ± 0.41%											
1	650	18.337	0.584	10.892	487.464	7944.15	29.4	9.9172988	0.006359	4.807694	16.886
2	730	0.526	0.299	9.191	766.818	4289.77	96.7	15.60066	0.002069	5.405597	18.975
3	810	0.524	0.368	13.739	1143.12	6126.52	97.6	23.25641	0.0017087	5.2346568	18.378
4	890	0.539	0.432	11.224	915.689	4936.12	97.0	18.62939	0.002504	5.2289311	18.358
5	970	0.639	0.197	7.58	615.476	3379.47	94.9	12.521661	0.0016989	5.2008761	18.26
6	1040	0.883	0.194	6.271	504.62	2851.32	91.5	10.266332	0.0020406	5.155075	18.1
7	1090	0.751	0.181	3.322	255.766	1520.75	86.8	5.2034773	0.0037563	5.1132858	17.954
8	1140	0.742	0.231	1.866	133.36	866.458	71.3	2.7131667	0.0091942	4.892944	17.184
9	1190	0.631	0.225	0.948	57.674	448.236	62.8	1.1733590	0.020707	4.613789	16.208
10	1240	0.516	0.243	0.434	15.996	188.047	24.0	0.3254334	0.0806366	2.4358059	8.575
11	1290	0.545	0.33	0.331	9.145	179.686	14.4	0.186052	0.191550	2.433528	8.567
12	1400	0.902	0.522	0.44	10.166	303.157	15.9	0.2068240	0.272573	4.318781	15.176
					Cumulative % ^{39}Ar rlsd =			100.00	Total gas age =		**18.14**
									Plateau age (steps 3-6) =		**18.27**
									Isochron age (steps (3-9) =		**18.50**

4 amu discrimination = 1.02879 ± 0.36%, $^{40}/^{39}K$ = 0.0001 ± 100.0%, $^{36}/^{37}Ca$ = 0.000288 ± 4.09%, $^{39}/^{37}Ca$ = 0.00071 ± 3.30%.
Isotope beams in mV, rlsd = released, error in age includes J error, all errors 1 sigma.
^{36}Ar through ^{40}Ar are measured beam intensities, corrected for decay for the age calculations.
*Temperature in centigrade.

Table 3. Average trace element concentration in representative core samples from the Kızıltepe Au-Ag deposit and outcrop samples from the Kızıltepe and surrounding gold prospects.

	Core samples from Arzu vein				**Outcrop samples from Kızıltepe area and other prospects**			
	Number of samples = 222*				Number of samples = 1144			
Elements	Range		SD	Average	Range		SD	Average
	From	To			From	To		
Au (g/t)	0.1	33	4	1.6	**0.005	23,500	2321	817
Ag (g/t)	0.2	754	90	33.2	0.01	251	20	10
Cu (ppm)	2	89	8	8	1	119	9	9
Pb (ppm)	2	740	111	40	2	516	19	12
Zn (ppm)	3	134	20	38	2	425	29	10
As (ppm)	2	2370	221	101	2	6500	400	193
Sb (ppm)	2	366	37	15	2	5270	224	37

*Source of data: unpublished reports for Galata Madencilik A.S., Turkey, 2007.
SD: Standard deviation. **Au values at Kızıltepe and other prospects are in ppb.

0.23, respectively. Average potassium values in the fresh volcanic rocks, argillized-silicified wall rocks and quartz veins at the Kızıltepe deposit and the prospects are 3.5%, 3.6% and 0.1%, respectively. The wall rock at Kızıltepe and the prospects is enriched in Au, Ag, As, Hg, W, and Zn by factors of 9, 2, 9, 8, 5, and 6, respectively.

Average trace element concentrations and geochemical relationships between Au-Ag and associated elements from mineralized epithermal quartz veins at Kızıltepe and the prospects are presented in Table 3 and Figures 19 and 20. Data from the Kızıltepe deposit show a moderate to strong association of Au with Cu and Ag contents in core samples of ore-grade and non-ore-grade material (Table 4a and Figure 19; correlation coefficients are greater than 0.58), whereas data from outcrop samples at Kızıltepe and the prospects display a moderate association of Au with Ag and no association of Au with Sb and Cu (Table 4b and Figure 20).

In epithermal systems with Ag/Au ratios of about 1 (as at Ovacık; Yılmaz *et al.* 2007), they contain mainly electrum and free gold (Cole & Drummond 1986). Au values in the Arzu vein range from 0.1 g/t to 32.5 g/t with an average of 1.6 g/t Au, whereas Ag contents are between 0.2 and 754 g/t with an average of 33.2 g/t Ag. The average Ag/Au ratio in the core samples of the Arzu south quartz vein is 22, with a range from 1 to 137. In the Arzu South vein, the highest Ag grade (754 g/t Ag) coincides with the highest Au grade (32.5 g/t Au), yielding an Ag/Au ratio of 23. The current resource estimate for the Kızıltepe deposit stands at approximately 2,111,847 Mt @ 2.8 g/t Au, 44 g/t Ag, yielding an Ag/Au ratio of about 16. Outcrop samples also returned an Ag/Au ratio of about 12. Seventy-eight rock-saw and rockchip samples from the Karakaya vein at the Kepez prospect returned average Au and Ag values of 3.34 g/t and 26.4 g/t, respectively, with an Ag/Au ratio of 8 (Galata Madencilik Company Report 2006). All these results show that Ag predominates over Au in the Sındırgı area.

10. Fluid inclusion studies

10.1. Fluid inclusion and types

Homogenization temperatures (Th) and final ice-melting temperature (Tm-ice) for quartz were obtained only from primary fluid inclusions. Their origins are distinguished using criteria provided by Roedder (1984) and Goldstein and Reynolds (1994). Microthermometric measurements were performed on inclusions with varying colors ranging from gray through purple to milky quartz crystals and chalcedonic quartz. However, most fluid inclusions studied were hosted by medium to coarse crystalline quartz (0.2 to 2.2 mm in grain size) with massive, vug-infill, and carbonate replacement texture pseudomorphed by quartz and by lesser chalcedonic quartz with crustiform banded quartz textures. Most samples contained well-constrained fluid inclusion assemblages (FIAs; Figure 21A), and in most cases the FIAs could be placed into an accurate paragenetic framework (Figures 21A and 21B). That is, the FIAs could be related to a specific event (growth zone or mineralization stage; Figure 21C). FIAs were all

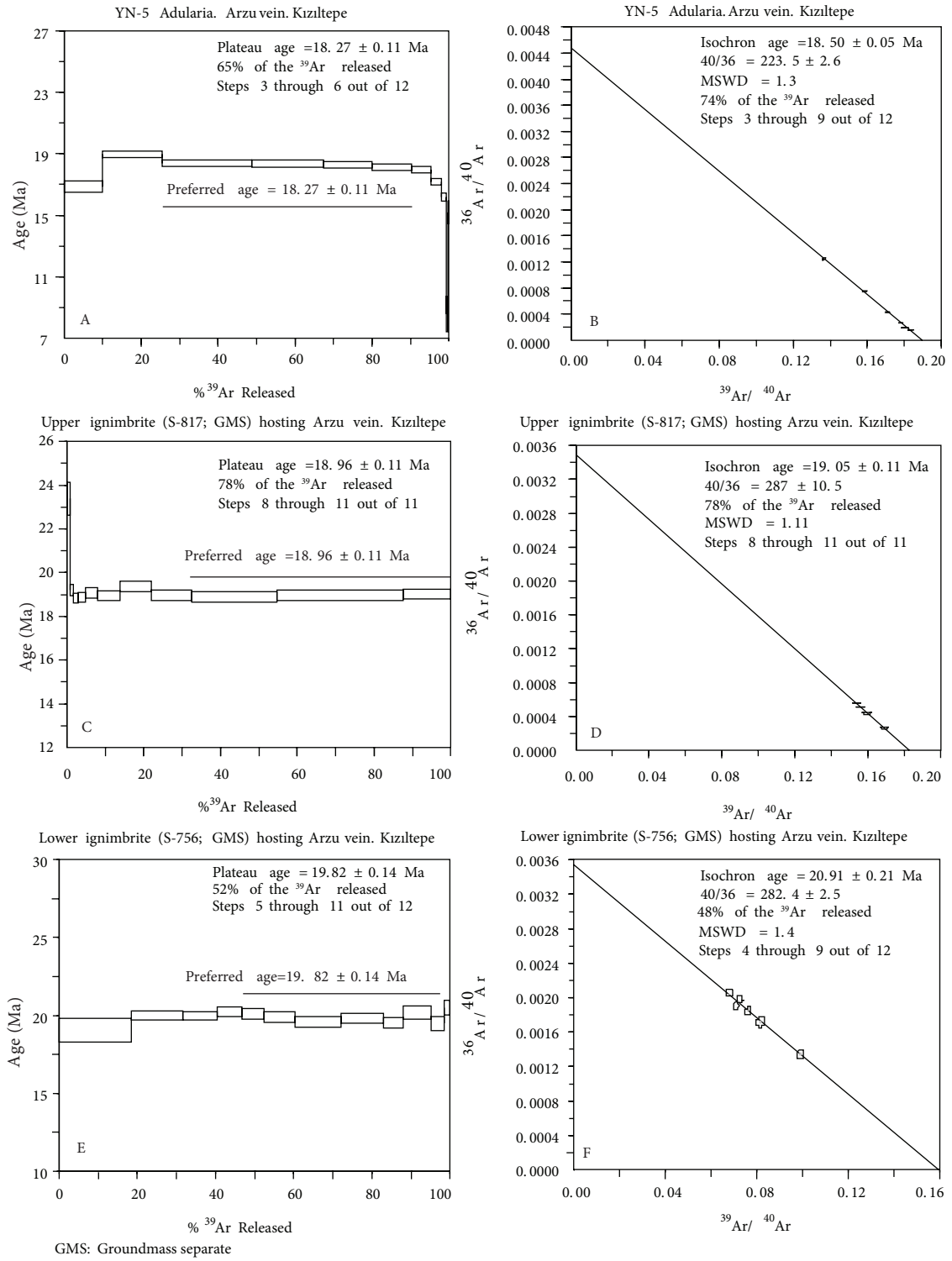

Figure 15. Step-heating spectra of adularia from the Kızıltepe gold deposits, and associated ignimbrites.

trapped approximately contemporaneously at a similar temperature and pressure and all trapped a fluid of the same composition (Goldstein & Reynolds 1994; Bodnar 2003; Goldstein 2003).

Coarse quartz crystals in the Kızıltepe Au deposit are zoned, with gray quartz in the core and translucent quartz in the outer rim (Figures 21D and 21E). The quartz crystals contain well-defined FIAs of primary, pseudosecondary,

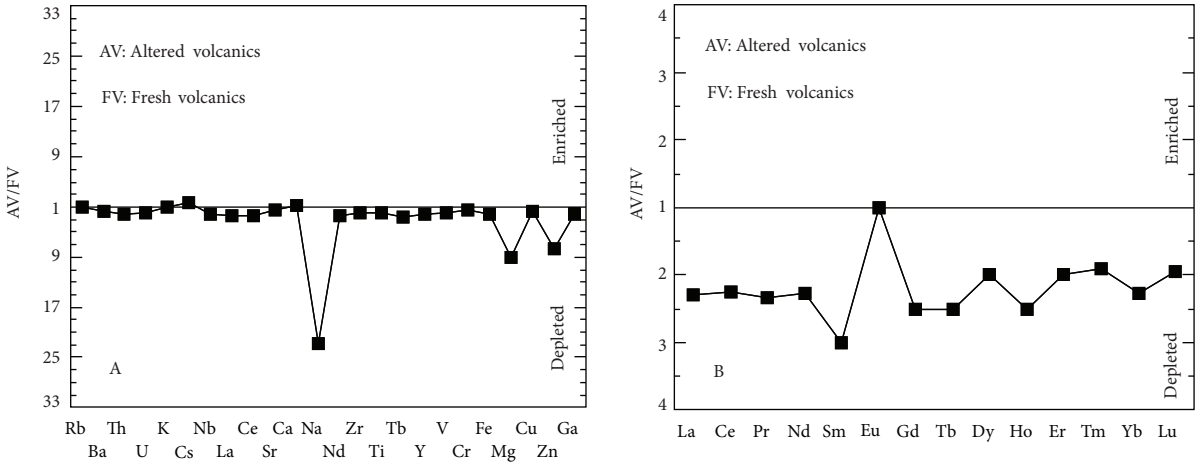

Figure 16. Plot of (A) major and trace elements and (B) REEs in altered wall rock at the Kızıltepe gold deposit and the prospects, normalized against fresh volcanic rocks.

and secondary inclusions. The coarse-grained quartz crystals contain both two-phase (vapor-rich) vapor-liquid (Figure 21F) and one-phase vapor inclusions (Figure 21F and 21G), whereas medium-grained quartz crystals host mainly liquid-rich inclusions (Figure 21H). The chalcedonic quartz contains generally two-phase liquid-vapor inclusions that represent a later generation of relatively higher salinity fluids (Figure 21B). Secondary two-phase liquid-vapor inclusions along trails may start in the light growth zone and extend into the core of the coarse crystalline quartz.

Fluid inclusions in quartz were very small (5-40 μm) and were, therefore, difficult to examine under the microscope. In the 15 samples from the Kızıltepe deposit and prospects, 193 of the primary fluid inclusions in the present study yielded what we consider to be reliable homogenization (Th) and final ice melting (Tm-ice) temperature measurements.

Two-phase vapor-rich (80 vol.% vapor (V) and 20 vol.% liquid (L)) (Figure 21F) and one-phase vapor (100 vol.% vapor; Figure 21G) two-phase liquid-rich (20 vol.% vapor (V) and 80 vol.% liquid (L)) (Figure 21H) inclusions were recognized in the study area, respectively. Single-phase, liquid-filled inclusions were not observed, which suggests that vapor-filled inclusions were formed by vapor-phase trapping rather than necking (Bodnar *et al.* 1985). The very small fluid inclusions in the chalcedonic quartz were unsuitable for microthermometric analysis and it is likely that they present a record of subsequent events (Fournier 1985). In spite of very small fluid inclusions in chalcedonic quartz from the Kızıltepe deposit, some were conducive to further study. The zonal distribution of primary

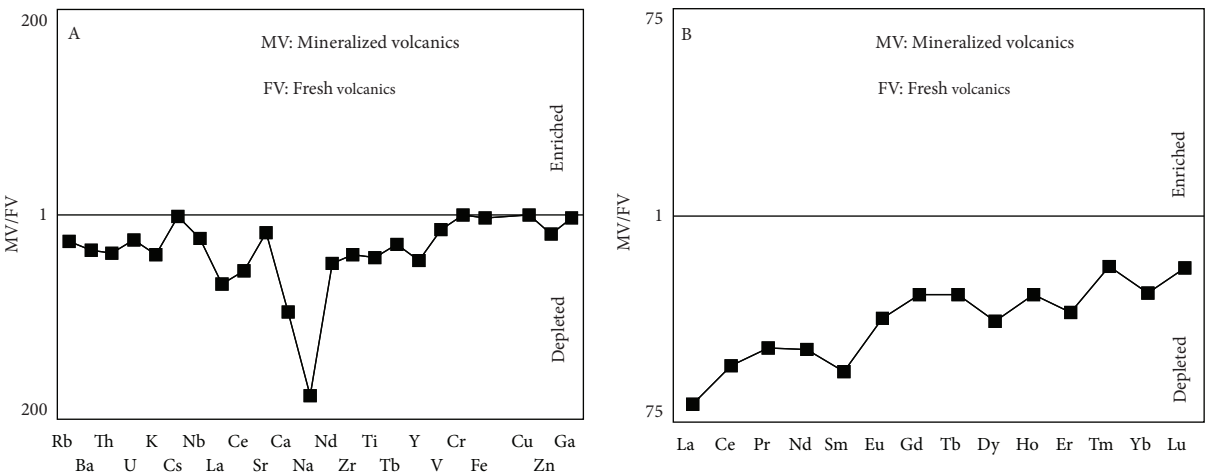

Figure 17. Plot of (A) major and trace elements and (B) REEs in quartz veins at the Kızıltepe gold deposit and the prospects, normalized against fresh volcanic rocks.

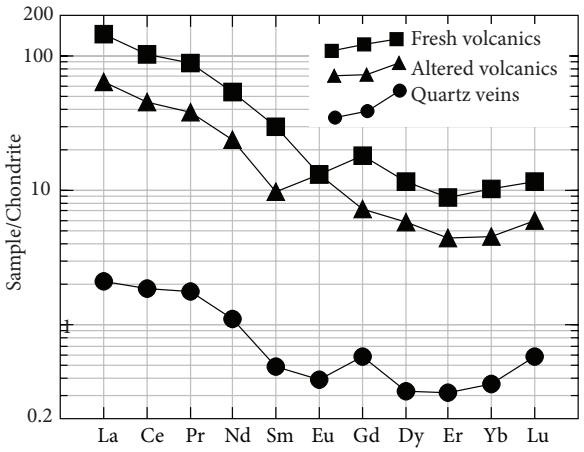

Figure 18. Plot of chondrite-normalized REE concentrations of fresh volcanic rocks, altered wall rock, and gold-mineralized quartz veins from the Kızıltepe prospect areas. Figure shows chondrite-normalized REE concentrations in the above-mentioned rocks. Normalized values are after Nakamura (1974).

inclusions (Figure 21C) indicates that entrapment of the fluid inclusions occurred during specific stages in the growth of quartz crystal. Vapor-rich inclusions trapped within the cores of the quartz crystals are often relatively small and have perfect negative crystal shapes. Liquid-rich inclusions occur in some instances as isolated inclusions (Figure 21H) in weakly defined crystal growth zones.

The apparent salinities of hydrothermal fluids are sensitive to variations in both their gas and salt contents because each contributes to the total freezing-point depression of the liquid (Hedenquist & Henley 1985). However, no liquid CO_2 could be observed at room temperature, nor are clathrates recognized by microthermometry, indicating that the CO_2 content is below 3.7% (Hedenquist & Henley 1985). The salinities of the studied inclusions (in wt.% NaCl equiv.) were calculated from the ice-melting temperatures, using the equation presented by Bodnar (1993). Therefore, salinities have not been corrected for the potential of dissolved CO_2 on freezing point depression for the Kızıltepe deposit or the prospects.

10.2. Microthermometry

Our fluid inclusion study suggests boiling due to the presence of variable vapor/liquid ratios, ranging from 20 to 100 vol.% (Figures 21C-21E). This observation is also consistent with the presence of lattice-bladed carbonate replacement pseudomorphed by quartz, lattice-bladed calcite and colloform/crustiform banding textures,

Table 4. a) Matrix of correlation between measured variables for Arzu vein in the Kızıltepe Au-Ag deposit; b) matrix of correlation between measured variables from the outcrop of Kızıltepe and from surrounding prospects in the Sındırgı region.

a)

Variables	Au	Ag	Cu	Pb	Zn	As
Sb	0.5	0.41	0.42	–0.05	–0.18	0.97
As	0.45	0.36	0.39	–0.05	–0.17	
Zn	–0.21	–0.2	–0.11	0.13		
Pb	–0.05	–0.05	–0.02			
Cu	0.58	0.66				
Ag	0.81					

b)

Variables	Au	Ag	Cu	Pb	Zn	As
Sb	–0.03	–0.02	0.14	0.14	0.1	0.37
As	–0.01	–0.04	0.35	0.15	0.13	
Zn	–0.03	–0.02	0.08	0.08		
Pb	–0.06	–0.08	0.11			
Cu	0.01	0.01				
Ag	0.69					

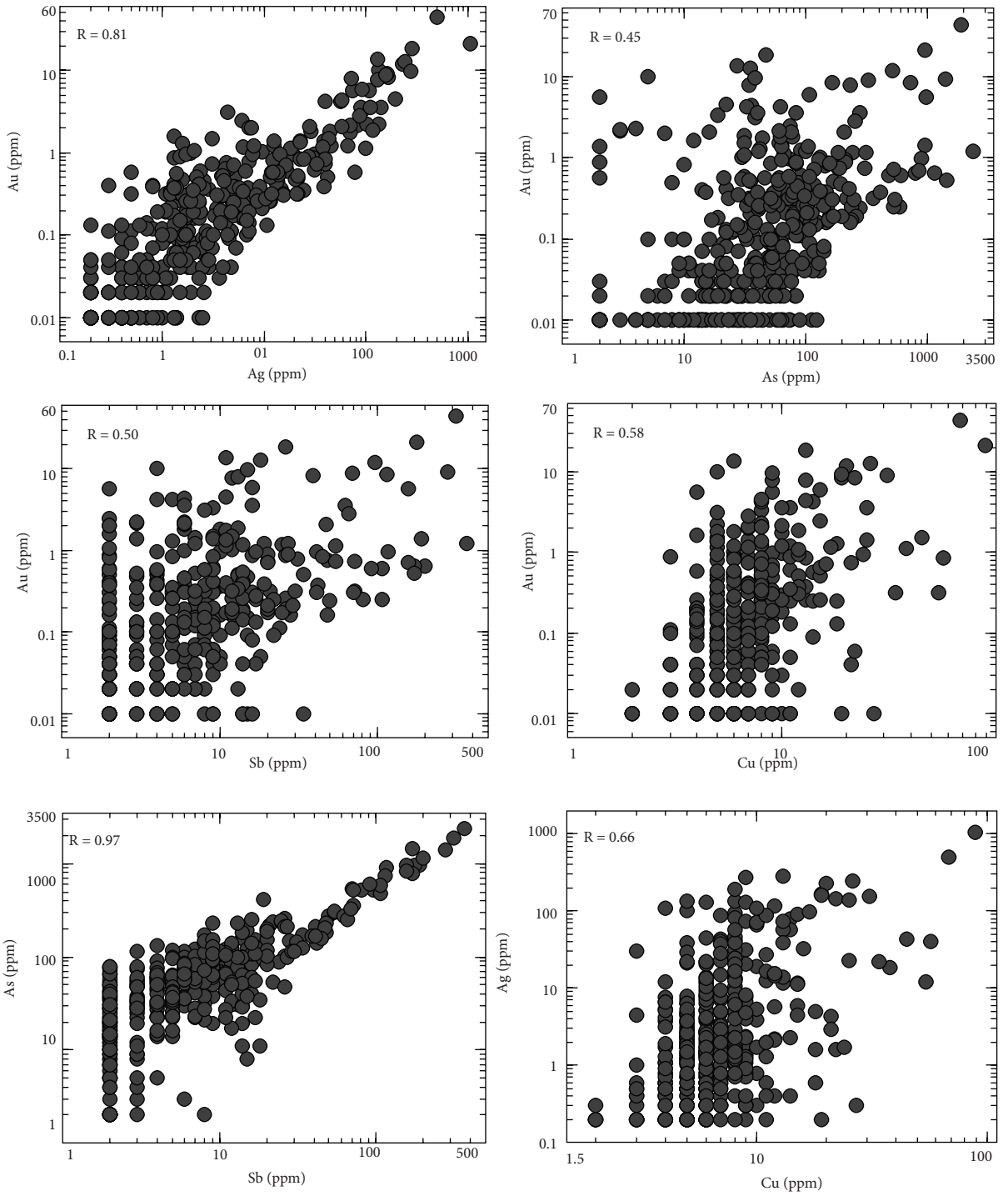

Figure 19. Log-Log plot of concentrations of Au-Ag, Au-As, Au-Sb, Au-Cu, As-Sb, and Ag-Cu in outcrop and drill core samples from the Kızıltepe deposit.

extensive hydrothermal brecciation, and adularia in quartz veins. Textural and fluid inclusion evidence suggested that boiling is the most important process in precious metal deposition (Drummond & Ohmoto 1985; Hedenquist & Henley 1985; Simmons & Christenson 1994; Stefansson *et al.* 2007). The studied inclusions show that boiling

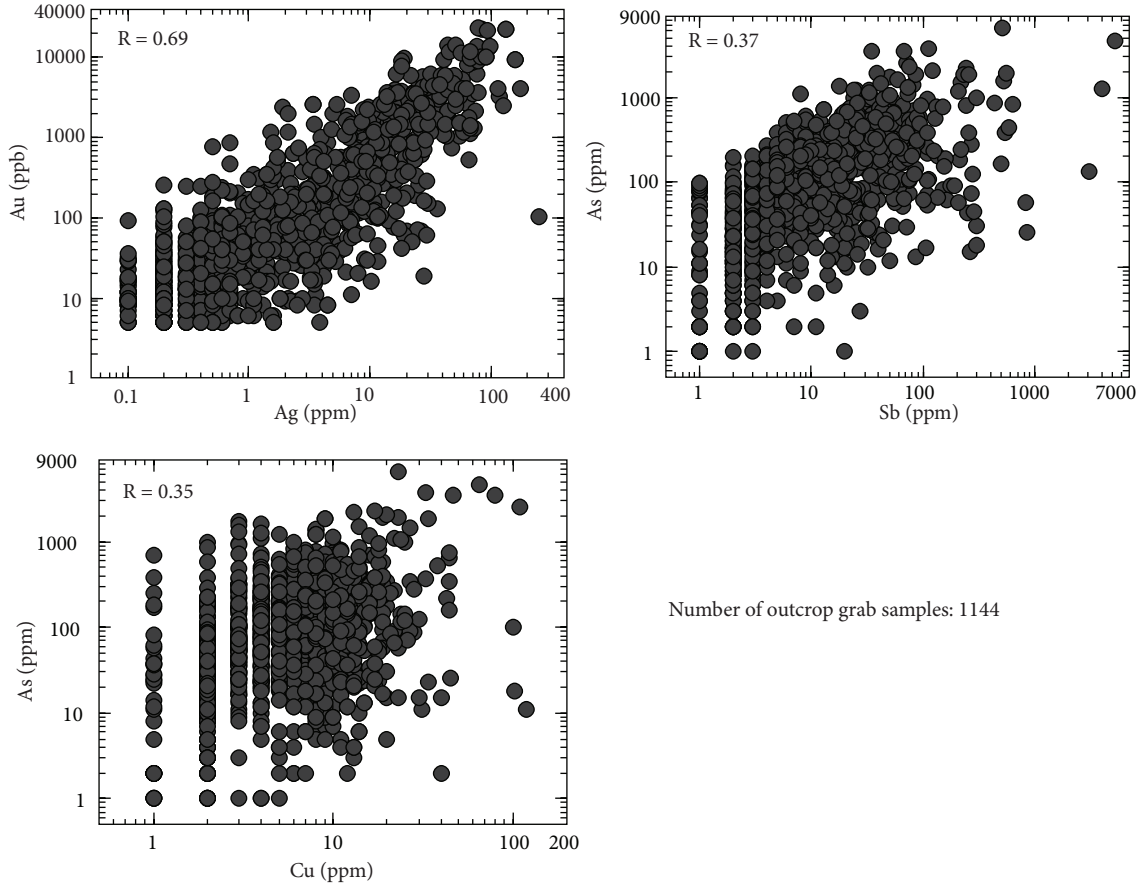

Figure 20. Log-Log concentrations of Au-Ag, As-Sb, and As-Cu in outcrop samples from prospects and surrounding grounds from the Sındırgı region.

hydrothermal fluids were trapped on the boiling curve (Bischoff & Rosenbauer 1985; Heinrich *et al.* 2004), and, therefore, no pressure correction for temperature was necessary (Potter 1977; Roedder & Bodnar 1980).

Homogenization temperatures, salinities, and first-melting temperatures are summarized and illustrated in Table 5 and in Figures 22 and 23. Fluid inclusions of primary origin in coarse crystalline quartz (Ore-stage Phase I) in the Au-Ag-rich Arzu South vein from the Kızıltepe deposit show Th ranging between about 305 and 395 °C, with a cluster between 350 and 375 °C, whereas they range from 157 to 330 °C with a cluster between 170 and 250 °C for medium-grained quartz (Figures 22A and 22B; Ore-stage Phase II). Fluid inclusions from chalcedonic quartz with crustiform textures returned Th values ranging from 150 to 241 °C. Salinities from coarse crystalline quartz in the Arzu South vein range from 1.1 to 3.4 wt.% NaCl equivalent, whereas they are between 0.4 and 2.4 wt.% NaCl equivalent in the medium-grained quartz. Fluid inclusion salinities from the late-stage chalcedonic quartz range from 3.6 to 4.8 wt.% NaCl equivalent (Figure 22).

Fluid inclusions from massive to hydrothermally brecciated quartz from the Kepez quartz vein system homogenize between 170 and 330 °C, with a cluster between 180 and 230 °C. Low salinity inclusions from the Kepez prospect range from 0.4 to 4.8 wt.% NaCl equivalent and are mainly between 0.4 and 2.8 wt.% NaCl equivalent (Table 5, Figure 22B).

The Th of fluid inclusions in quartz samples at the Kavaklıdüz prospect range from 195 to 312 °C, with a cluster between 220 and 290 °C (Figure 22C). The Th of these inclusions in samples of lattice-bladed quartz after calcite from the Karadüz prospect are in the range of 207 to 300 °C, with a cluster between 242 and 263 °C. The salinity from the Kavaklıdüz prospect ranges from 0.2 to 4.7 wt.% NaCl equivalent, with a cluster at 0.4 and 2.0 wt.% NaCl equivalent. At the Karadüz prospect salinity ranges from 0.5 to 3.1 wt.% NaCl equivalent, with a cluster between 0.5 and 2.0 wt.% NaCl equivalent (Figure 22C).

In this study, the first melting temperatures in the quartz-hosted inclusions in all samples from the Sındırgı area range from −33 to −21 °C.

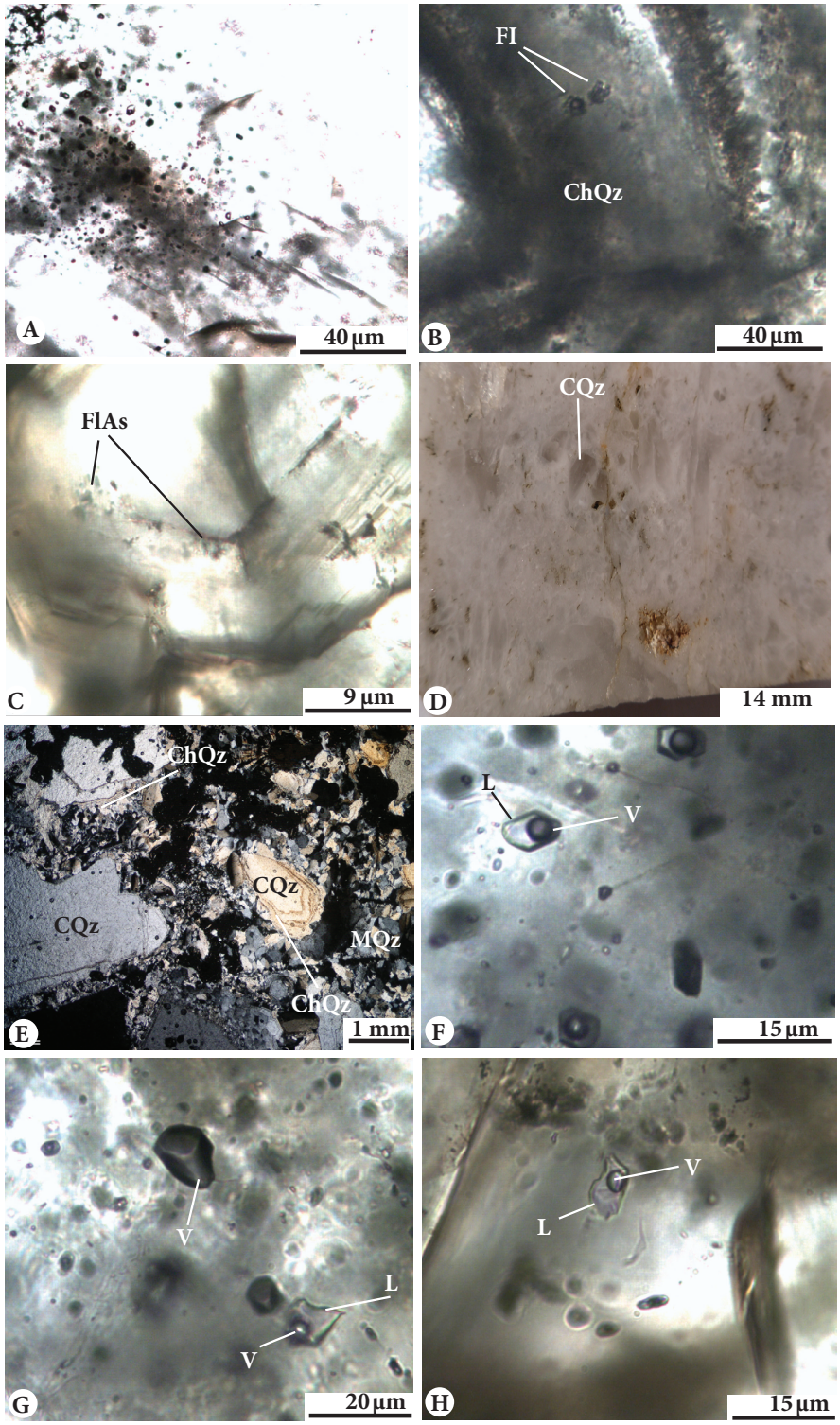

Figure 21. Photographs showing examples of fluid inclusion "classic" evidences of boiling in epithermal deposits, from the Kızıltepe veins of the Sındırgı District, western Turkey: (A) Coarse crystalline gray quartz core surrounded by a relatively clear medium-grained quartz rim, (B) micrograph of coarse crystalline quartz (CQz) within a matrix of medium-grained crystalline quartz (MQz) and coarse crystalline quartz overgrown by chalcedony quartz (ChQz), (C) chalcedony quartz with very few measurable fluid (FI) inclusions, (D) zoned coarse crystalline quartz with several growth bands marked by primary FIAs, (E) primary fluid inclusions within the core of coarse crystalline quartz, (F) vapor- and liquid-rich two-phase inclusions (closer view from E), (G) rarely occurring large vapor-dominated (V) and liquid-rich (L) fluid inclusion surrounded by mostly two-phase liquid-vapor inclusion associations (FIAs), and (H) liquid-rich fluid inclusion in medium-grained quartz (L: liquid, V: vapor).

Table 5. Microthermometric data of fluid inclusions from the Sındırgı area.

Deposit	Mineral	Number of analyses	Homogenization temperature (Th, °C)			Final ice melting (Tm-ice, °C)			Salinity (wt. % NaCl equiv.)			First melting temperature (°C)
			Min	Max	Mean	Min	Max	Mean	Min	Max	Mean	
Kızıltepe Deposit												
Arzu South vein	Coarse-grained quartz	11	305	395	354	−1.0	−2.0	−1.3	1.1	3.4	2.6	From −20 to −33 (11 analyses)
	Medium-grained quartz	85	157	330	231	−0.2	−1.4	−0.6	0.4	2.4	1.1	
	Chalcedony quartz	4	150	241	188	−2.1	−2.9	−2.7	3.6	4.8	2.5	
Kepez Prospect												
Kepez veins	Medium-grained quartz	21	170	330	223	−0.3	−2.9	−0.8	0.4	4.8	1.6	From −25 to −27 (3 analyses)
Kavaklıdüz Prospect												
Kavaklıdüz veins	Medium-grained quartz	54	195	312	253	−0.1	−2.8	−1.2	0.2	4.7	2.1	No data
Karadüz Prospect												
Karadüz veins	Medium-grained quartz	18	207	300	251	−0.3	−1.8	−0.8	0.5	3.1	1.4	No data

11. Discussion and results

11.1 Tectonic setting and structural model

In high-sulfidation epithermal deposits, hydrothermal activity closely follows deposition of volcanic host rocks by 0.1 to 0.5 m.y.; examples are Cerro Millo, Peru (Henning *et al.* 2008) and Rodalquilar, Spain (Arribas *et al.* 1995). Echavarria *et al.* (2006) suggested that there is commonly a time gap ranging from 0.5 to more than 3 m.y. between deposition of the youngest volcanic rocks and mineralization in other epithermal deposits; examples are Caylloma and Orcopamp, Peru (Echavarria *et al.* 2006); Ovacık, Turkey (Yılmaz *et al.* 2007); and Hishikari, Japan (Etoh *et al.* 2002; Hosono & Nakano 2003). The age data presented here suggest that mineralization in the area took place approximately 18 Ma ago, about 0.7 m.y. later than the youngest ignimbrite unit (Figure 15), in volcanic rocks 19.82 ± 0.14 Ma (lower ignimbrite) to 18.96 ± 0.11 Ma (upper ignimbrite) in age. Despite the age difference, it is probable that volcanism and mineralization were related to the same protracted magmatic event. Hydrothermal activity responsible for the formation of epithermal deposits is commonly initiated a short time after associated silicic volcanism, e.g., the dacitic Lower ignimbrite. These findings are in line with those of Yılmaz *et al.* (2007) and in contrast with earlier suggestions (Zanchi *et al.* 1990, 1993) that the rocks, and implicitly the deposits, are of approximately Mid-Late Miocene age. Economically significant gold-bearing quartz veins of the Kızıltepe deposit appear to be related primarily to NW-SE structures. The configuration of these mineralized structures forming echelon arrays suggests that the area was undergoing dextral normal deformation at the time of vein formation. Of five gold deposits in western Turkey, those of current economic importance occur in quartz vein systems (Ovacık/Bergama, Efemçukuru/İzmir, Kızıltepe/Sındırgı) and base metal-Au-quartz veins (Şahinli/Lapseki) with strong E-W and NW-SE trends (Yılmaz *et al.* 2007, 2010). Other deposits of this type should be sought with similar tectonic setting.

11.2. Implications of mineralogy and geochemistry

The Kızıltepe Au-Ag deposit is a notable example of a quartz ± calcite ± adularia ± illite type of low-sulfidation epithermal gold system. The deposit is characterized by the presence of chalcedonic to crystalline quartz, adularia, illite, and mixed-layered illite/smectite minerals, along with dominant crustiform banding and lattice-bladed carbonate replacement (pseudomorphed by quartz) textures. Temperature estimates for the systems at Kızıltepe and the prospects are summarized in Figures 22-24. Mineralization at Kızıltepe, Kepez, Kavaklıdüz, and Karadüz formed mainly at temperatures of about 220-300 °C, based on the presence of illite (with high crystallinity index; cf. Henley & Ellis 1983; Reyes 1990) and average fluid inclusion Th.

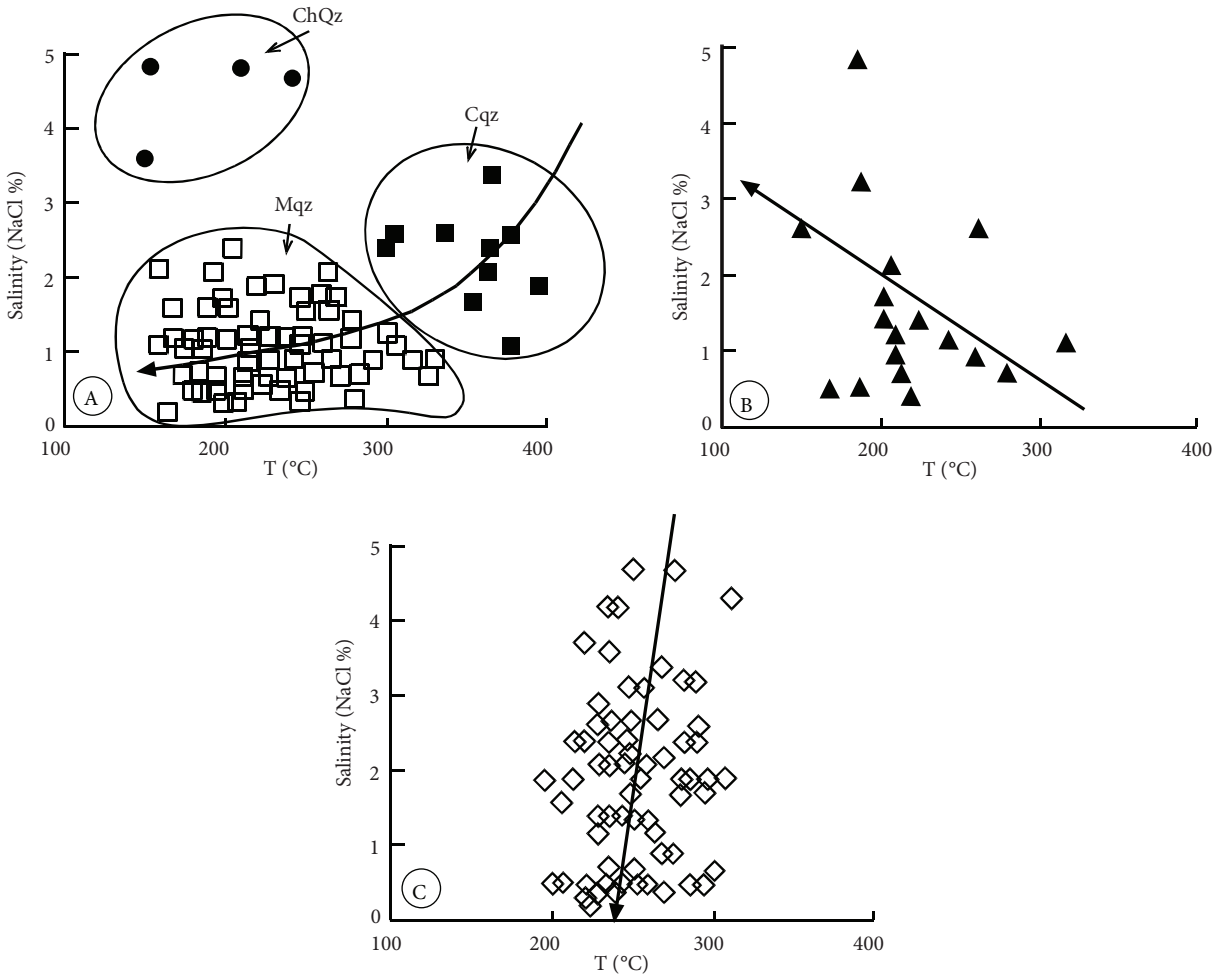

Figure 22. Homogenization temperatures and weight % NaCl equivalent salinity data for vein samples selected from: (A) Kızıltepe Au-Ag deposit, (B) Kepez prospect area, and (C) Kavaklıdüz and Karadüz prospect areas (CQz: coarse crystalline quartz, MQz: medium-grained quartz, ChQz: chalcedony quartz).

In the wall rock alteration zone at the Kızıltepe deposit, K and Ca display slight enrichments, while Na and Mg are depleted by factors of 23 and 9, respectively. K and Cs are enriched slightly in adularia or illite; Mg and Zn display a similar depletion pattern. Evidence for remobilization of REEs at the Kızıltepe deposit and the prospects is provided by their consistently decreasing values, starting from fresh volcanic rocks through montmorillonite-illite-altered wall rock and finally to quartz-adularia veins. Samarium shows weak negative anomalies in the altered volcanic rocks, probably inherited from major element removal from the volcanic rocks (Bierlein *et al.* 1999). This variation in Rb/Sr, following addition of K and Ca leaching of the wall rocks, is typical for alteration in shallow low-sulfidation hydrothermal systems (Yılmaz *et al.* 2007).

Moderate to strong positive correlation coefficients (R = 0.58 to 0.81) between Au and Cu, Au and Ag, and Ag and Cu suggest that all these elements are related to the same mineralizing event(s). In contrast, poor correlations between Au-As and Au-Sb or between Ag-As and Ag-Sb in the Kızıltepe core samples suggest that these elements (As and Sb) may relate to different stages of the mineralization event within the epithermal system. Arsenic and Sb occur generally at higher levels of epithermal systems, particularly at sinters or opaline-chalcedonic blankets, than those of Au and Ag (Corbett & Leach 1998). This is supported by a high correlation coefficient (R = 0.97) between As and Sb at Kızıltepe.

The ratios of Ag/Au are important in determining the type of dominant metal complexing and the expected metallogenic nature of the epithermal system (Cole & Drummond 1986). The Au (HS)–2 bisulfide complexes are very important for gold transport in the epithermal environment (Benning & Seward 1996; Seward & Barnes

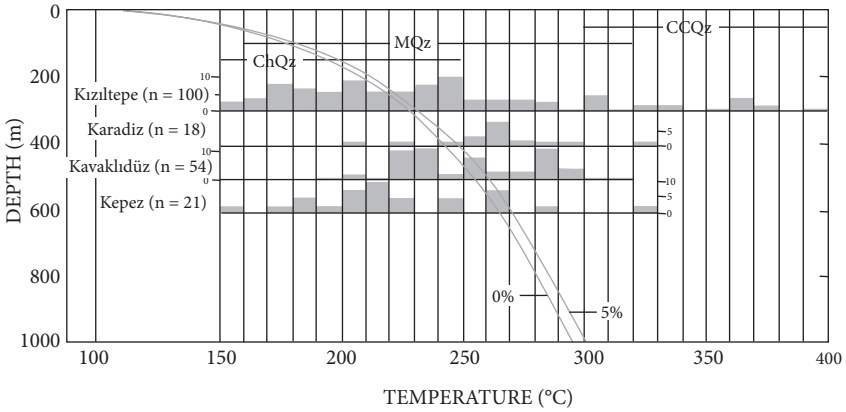

Figure 23. Histograms of fluid inclusion data from the Kızıltepe Au-Ag deposit and the Kepez, Kavaklıdüz, and Karadüz prospect areas, plotted on boiling point for depth curves of H_2O-NaCl (5 wt.% NaCl equiv.). The curves of pure H_2O and 5 wt.% NaCl are shown for reference (from Haas, 1971). The deposit and the prospect data were fitted at the mean Th values to the 5 wt.% NaCl curve as appropriate for measured salinities. These anomalously high temperatures (>300 °C) were recorded, but were attributed to mixed entrapment of liquid and vapor in boiling fluid inclusion populations (Cooke and Bloom, 1990).

1997). Thus, systems with Ag/Au ratios less than or equal to 1 tend to be dominated by native gold and electrum and sulfide complexing of Au, and show that homogenization temperatures of less than 250 °C are dominant (Pirajno 1992). Systems showing Ag/Au ratios greater than 1 (as in the Kızıltepe deposit) are characterized by argentite (achantite at Kızıltepe), base-metal sulfides and sulfosalts (silver compounds at Kızıltepe), and electrum, with minor Au. In such cases, chloride complexing is dominant and temperatures of homogenization are greater than 250 °C (Pirajno 1992). As indicated by the fluid inclusion data presented here, the average temperatures of formation of coarse-grained quartz (Ore-stage Phase I), medium-grained quartz (Ore-stage Phase II), and chalcedonic quartz (Ore-stage Phase III) at the Kızıltepe deposit are 354 °C (from 305 to 395 °C), 231 °C (from 157 to 330 °C), and 188 °C (from 150 to 241 °C), respectively. These overall temperature variations correspond with Ag/Au ratios ranging from 137 to 1 with an average of 22 at Kızıltepe. Variations in Ag/Au ratios may indicate that chloride complexing was dominant in the early stage, whereas sulfide complexing was dominant during the later stage of formation of the Kızıltepe epithermal system.

11.3. Composition of fluids

Fluid inclusions from Au-Ag-rich epithermal environments are mainly two-phase liquid and vapor (Roedder 1984; Bodnar *et al.* 1985; Shepherd *et al.* 1985) and show small freezing point depressions (Hedenquist & Henley 1985), indicating salinities of <1 to 2 wt.% NaCl equivalent. Salinity determinations indicate that quartz-hosted fluid inclusions from the Sındırgı Au-Ag deposit and prospects are similar (0.2-4.8 wt.% NaCl). No clathrates were observed using microthermometry, indicating that the CO_2 content is below 3.7% (Hedenquist & Henley 1985). The depression of first melting temperature down to −33 °C suggests the presence of at least minor MgCl (Crawford 1981; Davis *et al.* 1990). It is, therefore, likely that the Na^+ ($\pm Mg^{+2}$) cation(s) in the fluid or the NaCl–H_2O system (or the NaCl–MgCl–H_2O system) was dominant during Au-Ag mineralization (Davis *et al.* 1990).

Comparison of Th versus salinity for the mineralization in the Sındırgı district (Figure 22) indicates the presence of a similar, low-salinity fluid at generally similar temperatures (~300 °C, ~1.4-2.6 wt.% NaCl equivalent) in the Kızıltepe deposit and at the Kepez, Kavaklıdüz, and Karadüz prospects, except for the lower temperatures from Ore-stage Phase III. However, significant elevations in Th are recorded in the coarse crystalline quartz (Ore-stage Phase I) in the Kızıltepe deposit (Figure 22). This may be caused by intermittent pulses of higher temperature, low-salinity fluid (395 °C, 3.4 wt.% NaCl equiv.), as recorded during the growth of coarse quartz crystals (Figure 21). At the Kavaklıdüz and Karadüz prospect areas, a steep salinity increase within narrow Th intervals in the range of 200-300 °C indicates boiling with effervescence in a volatile-rich system (Hedenquist & Henley 1985; Wilkinson 2001). Fluid inclusion data from the Kızıltepe deposit suggest that the ore-forming fluids were generally of low salinity (<5 wt.% NaCl equivalent).

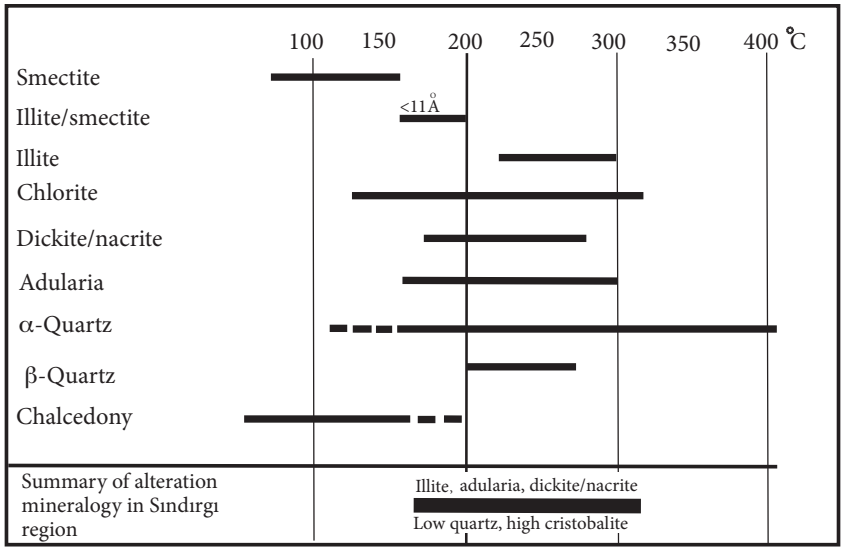

Figure 24. Generalized temperature estimates for the Kızıltepe deposit and the prospects, based on clay mineralogy proximal to and away from mineralized zones. Temperature ranges of the hydrothermal minerals are from Henley and Ellis (1983), Reyes (1990), and White and Hedenquist (1995).

11.4. Gold-silver deposition and depths of formation

Boiling is an important physical process affecting mineralization within low-sulfidation epithermal systems (Drummond & Ohmoto 1985; Hedenquist & Henley 1985). Boiling occurs in the ascent of fluids in most high permeability systems, whereas linear thermal profiles are common on the margins (Hedenquist *et al.* 1992). Studies of active geothermal systems (Brown 1978; Henley & Hedenquist 1986; Simmons & Christenson 1994) and thermodynamic studies (Drummond & Ohmoto 1985; Simmons & Brown 2000) have demonstrated that the presence of adularia and platy calcite, mostly pseudomorphed by quartz, is a strong indicator of boiling. The presence of hydrothermal breccias with associated platy or lattice-bladed calcite (commonly pseudomorphed by quartz) and colloform/crustiform textures in the Kızıltepe Au-Ag deposit and prospects, particularly in Stage II of Kızıltepe, is evidence for periods of sharp pressure drops. Apart from the mineralogical evidence, boiling in the Kızıltepe Au-Ag deposit and prospects is also demonstrated by the relationship between fluid inclusion homogenization (Th) and melting point (Tm-ice)/salinity data. The presence of liquid-rich to vapor inclusions with variable liquid-to-vapor ratios and relatively large ranges in homogenization temperatures at the Kızıltepe deposit and the prospects suggests boiling in the hydrothermal system (White & Hedenquist 1995). Boiling trends in the Sındırgı area are shown in Figure 22. Of these, trend 22A, obtained from the Kızıltepe Au-Ag deposit, is the combination of boiling of a volatile-rich fluid with subsequent dilution. The drop in salinity in the CQz area is due to the loss of volatiles, and the dilution trend in the MQz area relates to the volatile-poor (boiled) fluid (Hedenquist & Henley 1985; Wilkinson 2001), whereas trend 20B from the Kepez prospect indicates boiling in a volatile-free system. Trend 20C from the Kavaklıdüz and Karadüz prospects may be explained by boiling of volatile-rich fluids (Hedenquist & Henley 1985; Wilkinson 2001).

Most of the inclusions melt at an average of −0.6 to −1.3 °C, indicating apparent salinities of <2.6 wt.% NaCl (Figure 22A). There are also a few low- to moderate-temperature inclusions occurring in Ore-stage Phase III (Figure 22A) with moderate apparent salinities (3.6 to 4.8 wt.% NaCl equiv.). The co-existence of moderate-salinity inclusions with low-salinity inclusions may be explained by entrapment (Scott & Watanabe 1998) of variably saline fluids forming from the intense boiling of low salinity fluids (Simmons & Brown 1997).

The highest range of homogenization temperatures (305-395 °C, with a cluster between 350 and 375 °C) in Ore-stage Phase I from the Kızıltepe deposit is difficult to explain at epithermal depths under hydrostatic pressure (Figure 23). The maximum thickness of the volcanic succession in the Sındırgı area is about 500-600 m (Erkül *et al.* 2005; this study). These anomalously high temperatures (>300 °C) might be attributed to mixed entrapment of liquid and vapor in boiling fluid inclusion populations (Cooke & Bloom 1990; Figure 23). As stated previously in this study, there was no evidence of necking down for the samples under investigation. In other words, the high temperature

inclusions are not artifacts but represent influxes of high-temperature fluid into this hydrothermal system. Such a high-temperature fluid probably originated at deeper levels in the system and may reflect a hydrothermal regime associated with changes from hydrostatic to lithostatic pressure (Shamanian *et al.* 2004).

For hydrothermal deposits, homogenization temperatures represent only the lower limit of mineralization temperature and, therefore, the maximum of peak homogenization temperatures and the average ore-fluid salinity (5 wt.% NaCl equivalent) were used to estimate the depth of mineralization under hydrostatic conditions in the boiling temperature–depth diagram (Figure 23) of Haas (1971). The frequent occurrence of quartz breccias in the Sındırgı area is evidence of periodic excessive fluid pressure increase. Simmons (1991) noted that high-pressure conditions were not typical of steady-state hydrothermal activity. Due to disruption of permeability barriers, the high pressure decreased abruptly and, therefore, high-temperature fluid boiled. This may have resulted in a rapid temperature decrease to lower levels (from approximately 300 to 250 °C) and gas separation, causing the Au-Ag precipitation, particularly at the Kızıltepe deposit and the Kepez prospect. This process may have been repeated three times, as suggested by the three separate phases of mineralization recorded in the Kızıltepe deposit. Because boiling occurred at the Kızıltepe deposit and at the Kepez, Kavaklıdüz, and Karadüz prospects, it is not necessary to make a pressure correction to the measured homogenization temperatures. Consequently, most microthermometric data in the range of 170 to 280 °C represent the mineralization temperature. The steep dip of the Kızıltepe orebody, its association with steep extensional faults, and the open-space style of veining suggest that ore-forming fluids may have experienced transient periods of hydrostatic fluid pressure, and that the boiling is likely to have occurred at these times (Zhai *et al.* 2009).

Acknowledgments

The authors are grateful to Galata Madencilik San. & Tic. Ltd., the Turkish subsidiary of Ariana Resources plc, for financial and logistic assistance. J. Hedenquist, İlkay Kuşçu, and an anonymous reviewer are thanked for their invaluable comments in improving the quality of this paper.

Appendix

Appendix 1

Table 1.1. Summary of whole rock and clay mineralogy at the Kızıltepe Au-Ag deposit and the prospect areas.

Appendix 2

X-ray diffraction

Two analytical procedures were used for this study: 1) a standard procedure used to determine the mineral components of an unknown powdered sample, and 2) a technique known as the 'clay-adapted' procedure used to indicate the nature of the clay and main minerals present in the sample. The diffractometer used was an automated PW3710 instrument. The CuKα radiation source is supplied by a Cu tube from a graphite-back monochromator. Experimental conditions were: (a) for the spectra of powder in a pellet prepared from a sample crushed to <40 μm, 2θ scanning 4° to 9° for a velocity of 0.02° of 2θ/s; and (b) for clay fractions <2 μm on oriented sections, 2θ scanning of 2° to 36° for a velocity of 0.02° of 2θ/s and on a fixed sample, whereby each sample was analyzed untreated, treated with glycol, and heated to 500 °C for 4 h. The value of a peak width at half-height for the illite 001 XRD reflection is known as the Kubler index or the illite 'crystallinity' index. The first of the two measurements proposed by Eberl and Velde (1989) is the width at half-height of the 001 illite reflection (the half-height width of the 005 illite reflection works equally well), with the XRD background determined on the high 2θ angle side of the reflection, rather than as an average of the background on both sides of the reflection, as is used for the Kubler 'crystallinity' index (Eberl & Velde 1989). The background is measured in the former manner to avoid the reversal in values undergone by the 'crystallinity' index at the larger expandabilities when the background is measured with the traditional method. The second measurement is the Srodofi intensity ratio *(Ir)*, which is defined, using maximum illite XRD peak intensities, as: $Ir = [001/003]_{\text{air-lried}} - \sim - [001/003]_{\text{glycolated}}$. The peak widths were measured at half height and recalculated to Δ° 2θ to allow for the dependence of the peak width on the ratio of the diffractometer speed to chart speed (Brill 1988).

^{40}Ar/^{39}Ar dating

The samples were irradiated in-core for 7 h in the 5C position, surrounded by fuel rods on all four sides. J factors were determined by fusion of 3-5 individual crystals of neutron flow monitors, which gave reproducibility of 0.10% to 0.40% at each standard position. An error in J between 0.54% and 0.98% was used in age calculations. Samples analyzed by the furnace step-heating method utilized a double vacuum resistance furnace similar to the design

Table 1.1. Summary of whole rock and clay mineralogy at the Kızıltepe Au-Ag deposit and the prospect areas.

Sample no.	Elevation (m)	Whole rock and oriented clay analysis by XRD	Dickite/nacrite crystallinity index (mm)	Illite crystallinity index (mm)	Host rock description
SA-2	353	Quartz (low quartz), K-feldspar, illite, kaolinite (nacrite)	0.7	3	Argillitized and silicified ignimbrites with quartz stockwork
SA-6	347	Quartz (low quartz), K-feldspar, illite, kaolinite (nacrite)	0.5	3	Argillitized and silicified ignimbrites
SA-7	346	Quartz (low quartz), K-feldspar, illite, kaolinite (nacrite)	0.9	3	Argillitized and silicified ignimbrites
KEP-6	888	Quartz, K-feldspar, illite, kaolinite (nacrite)	0.8	3	Argillitized and silicified ignimbrites
KEP-7	844	Quartz, K-feldspar, illite, chlorite	0.8	1.5	Argillitized and silicified ignimbrites
SKAV-2	1225	Quartz, Na-feldspar, illite (trioctahedral), chlorite, kaolinite	-	2.5	Argillitized and silicified volcaniclastics
SKAV-6	1330	Quartz, K-feldspar, kaolinite (nacrite), illite	0.5	2.5	Argillitized and silicified volcaniclastics
Sample no.	**Drill core depth**				
C-18	70	Quartz, nacrite	0.8	-	Argillitized and silicified ignimbrites
C25	33	Quartz, K-feldspar, illite, kaolinite (dickite)	1	1	Argillitized and silicified ignimbrites
C-30	44	Quartz (high cristobalite), K-feldspar, illite/smectite, smectite, kaolinite (nacrite)	1	2	Argillitized and silicified ignimbrites

of Staudacher *et al.* (1978). Reactive gases were removed by three GP-50 SAES getters prior to being admitted to a MAP 215-50 mass spectrometer by expansion. Mass spectrometer discrimination and sensitivity was monitored by repeated analysis of atmospheric argon aliquots from an on-line pipette system. Measured $^{40}Ar/^{36}Ar$ ratios were 287.23 ± 0.36% during this work, and thus a discrimination correction of 1.02879 (4 AMU) was applied to measured isotope ratios. An age of 27.9 Ma (Steven *et al.* 1978; Cebula *et al.* 1986) was used for the Fish Canyon Tuff Sanidine flux monitor in calculating ages for samples.

For $^{40}Ar/^{39}Ar$ analysis, a plateau segment consists of three or more contiguous gas fractions having analytically indistinguishable ages (i.e. all plateau steps overlap in age at ±2s analytical error) and comprising a significant portion of the total gas released (typically >50%). Total gas (integrated) ages are calculated by weighting the amount of ^{39}Ar released, whereas plateau ages are weighted by the inverse of the variance. For each sample, inverse isochronal diagrams are examined to check for the effects of excess argon. Reliable isochrons are based on the MSWD criteria of Wendt and Carl (1991) and, as for plateaus, must comprise contiguous steps and a significant fraction of the total gas released. All analytical data are reported at the 1s confidence level.

Geochemical analysis

The detection limit for MgO, CaO, Na_2O, MnO, and Cr_2O_3 was 0.01%. Detection limits for SiO_2, Al_2O_3, K_2O, and Fe_2O_3 were 0.04, 0.03, 0.04, and 0.04 wt.%, respectively. Au has the lowest detection limit at 0.5 ppb. The detection limit for Ba, Co, Ga, Hf, Nb, Rb, Se, Sr, Zr, La, and Ce was 0.5 ppm, and for Eu, Gd, Dy, Ho, Er, Tm, and Yb was 0.05 ppm. The detection limit for Ag, Bi, Cd, Cs, Cu, Hg, Mo, Ni, Pb, Sb, Ta, Th, Tl, U, W, Y, Sm, Te, and Lu was 0.1 ppm. The detection limits are 100 ppm for Ti; 5 ppm for V; 1 ppm for Zn, As, Sc, Sn, and Zn; and 0.4 ppm for Nd. The detection limit for Pr is 0.02. Loss on ignition (LOI), C, and S were analyzed by LECO (macro carbon, hydrogen, nitrogen, sulfur analysis). Major and trace element concentrations were normalized to those of sample "PV". Sample PV represents the arithmetic mean of 2 samples with andesitic composition from the study area.

Fluid-inclusion microthermometry

For microthermometric analysis, doubly polished thin sections, approximately 100-200 μm thick, were prepared. Microthermometric measurements were carried out using a Linkam THMGS-600 heating-freezing stage at the Department of Geological Engineering, Dokuz Eylül University, İzmir, Turkey. The stage is mounted on a DM LM/P Leica microscope with a maximum magnification of 100× and fitted with a video camera and monitor. The stage has a temperature range from –196 °C (temperature of liquid nitrogen) to 600 °C. The systems were calibrated with synthetic fluid inclusions (supplied by the Institute of Geosciences, University of Leoben, Austria). The precision of low-temperature phase transitions (<10 °C) is 0.3 °C, with a maximum error of ±2 °C. Photomicrographs of the fluid inclusions were taken prior to microthermometric study in order to record the original vapor/fluid ratio for comparison with those which underwent heating and freezing processes.

Appendix 3

Table 3.1. Selected major and trace element geochemistry for samples from the Kızıltepe Au-Ag deposit and the prospect areas.

Table 3.1. Selected major and trace element geochemistry for samples from the Kızıltepe Au-Ag deposit and the prospect areas.

Sample	SiO_2	Al_2O_3	Fe_2O_3	MgO	CaO	Na_2O	K_2O	TiO_2	P_2O_5	MnO	Cr_2O_3	Ni	Sc	LOI	TOT/C	TOT/S	SUM	Ba	Be	Co
SKAV-1	71.48	0.47	0.42	1100	152,300	300	600	100	0.02	500	10	17	1	12	3.52	0.01	99.87	15.3	3	0.5
SA-2	69.62	15.06	2.66	3000	1500	3000	71,100	5600	0.06	100	20	11	10	3.9	0.09	0.26	99.73	1278.3	2	2.3
SA-7	75.4	10.93	2.99	900	800	2100	58,900	4100	0.14	100	10	10	7	3.6	0.1	0.39	99.75	1132.5	2	0.6
C-11	88.02	5.39	1.91	1900	1300	300	13,600	1700	0.09	200	10	13	3	2.6	0.08	0.6	99.91	114.1	2	3.2
KEP-1	97.97	0.52	0.77	200	800	200	500	100	0.02	100	30	15	1	0.6	0.03	0.09	100.06	32.6	2	0.5
SKAR-1	96.73	1.08	1.15	100	200	100	1100	300	0.01	100	10	12	1	0.9	0.04	0.02	100.06	25.1	5	0.7
SA-3	96.15	0.71	1.61	100	400	300	2100	100	0.05	100	20	5	1	1.1	0.03	0.1	99.92	82.7	3	0.6
C-1	97.66	0.67	0.77	200	200	300	800	100	0.01	100	20	11	1	0.8	0.02	0.07	100.06	19.7	1	1.5
C-22	97.8	0.73	0.62	100	200	100	500	100	0.02	100	10	7	1	0.8	0.01	0.01	100.06	21.2	2	0.6
C-28	98.17	0.35	0.65	100	200	100	400	100	0.01	100	10	5	1	0.8	0.01	0.01	100.06	8.1	2	0.7
S-753	66.02	15.32	4.18	15,600	31,700	32,400	35,550	5600	0.18	800	20	5	9	2	0.07	0.01	99.86	1131.5	3	7.6

Sample	Cs	Ga	Hf	Nb	Rb	Sn	Sr	Ta	Th	U	V	W	Zr	Y	La	Ce	Pr	Nd	Sm	Eu
SKAV-1	1.5	0.8	0.5	0.5	3.8	1	845.4	0.1	0.1	0.1	5	1.9	1.1	1.0	0.5	0.7	0.11	0.3	0.06	0.03
SA-2	8.6	16.5	6.1	14.5	267.7	3	99.8	1.1	15.9	4.1	60	19.6	205	24	37.5	67.0	7.14	23.3	4.22	1.23
SA-7	4.9	9.6	4.3	10.2	189.9	3	155.2	0.9	13.9	3.3	38	13.9	146	14.6	31.6	62.5	7.16	25.7	3.57	0.8
C-11	4.0	6.4	1.9	4.3	55.4	1	24.2	0.3	5	2.4	54	1.8	57.7	13.6	13.4	25.1	2.85	10.7	2.05	0.68
KEP-1	2.0	3.2	0.5	0.5	4	1	18.9	0.1	0.2	0.1	5	0.2	1.5	0.3	0.4	1.1	0.15	0.4	0.05	0.02
SKAR-1	0.6	12.9	0.5	1.1	7.7	1	5.1	0.1	1.7	0.4	6	0.5	14.1	1.6	1.7	3.8	0.47	1.6	0.31	0.07
SA-3	2.0	6.6	0.5	0.5	9.2	1	30.7	0.1	0.4	0.4	5	13.8	3.8	1	1.5	2.7	0.34	1.1	0.17	0.03
C-1	1.5	3.9	0.5	0.5	4.2	1	16.6	0.1	0.2	0.1	5	3.8	5.2	0.4	0.6	1.1	0.12	0.3	0.05	0.02
C-22	1.3	1.4	0.5	0.5	2.7	1	39.5	0.1	0.1	0.1	5	3	2	0.2	0.1	0.4	0.03	0.3	0.05	0.02
C-28	0.8	3.9	0.5	0.5	1.9	1	14.1	0.1	0.1	0.1	5	0.2	1.5	0.2	0.1	0.3	0.04	0.3	0.05	0.02
S-753	3.1	18.1	5.6	14.7	134	3	388.1	1.2	19.4	5	73	1.5	200	26.8	48.1	87.7	9.66	34	5.66	1.13

Sample	Gd	Tb	Dy	Ho	Er	Tm	Yb	Lu	Mo	Cu	Pb	Zn	Ni	As	Cd	Sb	Bi	Ag	Au	Hg
SKAV-1	0.19	0.03	0.09	0.03	0.06	0.02	0.05	0.01	0.3	2	0.5	2	1.2	0.9	0.1	0.3	0.1	0.3	97.6	0.01
SA-2	3.46	0.68	3.86	0.74	2.1	0.35	2.17	0.34	0.3	3	22	6	2.4	56.1	0.1	3	0.1	0.6	11.5	0.16
SA-7	2.59	0.47	2.42	0.46	1.35	0.22	1.44	0.23	0.6	4	20	4	1.6	97.2	0.1	2.4	0.1	0.6	125.7	0.02
C-11	2.15	0.41	2.1	0.42	1.09	0.17	1.03	0.15	0.8	3	13	14	3.1	34	0.1	0.3	0.1	0.8	21.6	0.01
KEP-1	0.09	0.02	0.05	0.02	0.03	0.01	0.05	0.01	4.1	3	2	2	6.1	5.2	0.1	14	0.1	48.1	14,278	0.1
SKAR-1	0.39	0.06	0.29	0.06	0.16	0.05	0.19	0.04	0.8	3	2	1	2.6	58.1	0.1	9.6	0.1	0.3	60.4	0.06
SA-3	0.27	0.04	0.16	0.03	0.11	0.02	0.07	0.02	2	4	3	9	3	86.9	0.1	3.9	0.1	14.1	985.1	0.01
C-1	0.11	0.02	0.05	0.02	0.04	0.01	0.06	0.01	0.6	5	0.6	1	3	2.2	0.1	0.3	0.1	1.8	27.8	0.01
C-22	0.05	0.01	0.05	0.02	0.03	0.01	0.05	0.01	0.7	7	2	2	2.8	2.2	0.1	7.7	0.1	100	1458.4	0.01
C-28	0.05	0.01	0.05	0.02	0.03	0.01	0.05	0.01	0.5	2	0.6	1	1.4	11.1	0.1	1.7	0.1	2.3	184.4	0.03
S-753	4.65	0.87	4.27	0.87	2.49	0.38	2.28	0.39	0.8	5	13	53	4.5	4.8	0.1	0.1	0.1	0.3	6.8	0.01

SKAV-1: Kavaklıdüz altered volcanic; SA-2, SA-7: Altered wall rock of the Arzu vein (Kızıltepe) outcrop; C-11: Altered wall rock of the Arzu vein (Kızıltepe) core sample; KEP-1: Outcrop vein from the Kepez prospect; SKAR-1: Outcrop vein from the Karadüz prospect; SA-3: Quartz from the Arzu vein (Kızıltepe); C-1, C-22, C-28: Quartz core sample from the Arzu vein (Kızıltepe); S-753: Fresh volcanic rock. For Mo, Cu, Pb, Zn, Ni, As, Cd, Sb, Bi, Ag, Au, Hg, Tl, and Se, a 0.5 g sample was leached with HCl-HNO3-H_2O at 95 °C and analyzed by ICP-MS. Au in ppb; limit for remaining elements 0.2 g sample fused by $LiBO_2$ and analyzed by ICP-AES. SiO_2, Al_20_3, Fe_2O_3, P_2O_5, LOI, TOT/C, SUM in wt %; MgO, CaO, Na_2O, MnO, K_2O, and TiO_2 in ppm.

References

Akay, E. 2009. Geology and petrology of the Simav Magmatic Complex (NW Anatolia) and its comparison with the Oligo-Miocene granitoids in NW Anatolia: implications on Tertiary tectonic evolution of the region. *International Journal of Earth Sciences (Geol Rundsch)* **98**, 1655–1675.

Akay, E. & Erdoğan, B. 2001. Formation of subaqueous felsic domes and accompanying pyroclastic deposits on the Foça Peninsula (Izmir, Turkey). *International Geology Review* **43**, 661–674.

Akay, E. & Erdoğan, B. 2004. Evolution of Neogene calc-alkaline to alkaline volcanism in the Aliaga–Foca region (Western Anatolia, Turkey). *Journal of Asian Earth Science* **24**, 367–387.

Aldanmaz, E. 2006. Mineral-chemical constraints on the Miocene calc-alkaline and shoshonitic volcanic rocks of western Turkey: disequilibrium phenocryst assemblages as indicators of magma storage and mixing conditions. *Turkish Journal of Earth Sciences* **15**, 47–73.

Aldanmaz, E., Pearce, J., Thriwall, M.F. & Mitchell, J. 2000. Petrogenetic evolution of late Cenozoic, post-collision volcanism in western Anatolia, Turkey. *Journal of Volcanology and Geothermal Research* **102**, 67–95.

Altunkaynak, S. & Yılmaz, Y. 1998. The Mount Kozak magmatic complex, Western Anatolia. *Journal of Volcanology and Geothermal Research* **85**, 211–231.

Arribas, A. Jr., Cunningham, O., Rytuba, J., Rye, O., Kelly, W., Podwysocki, W., McKee, E. & Tosdal, R. 1995. Geology, geochronology, fluid inclusions, and isotope geochemistry of Rodalquilar Au alunite deposit, Spain. *Economic Geology* **90**, 795–822.

Aygün, O. & Çolakoğlu, A.R. 2008. Kızıltepe (Sındırgı-Balıkesir) altın cevherleşme bölgesi dere sedimanı örneklerindeki tane boyutunun altın analiz değerlerine etkisi. *Hacettepe Yer Bilmleri Dergisi* **29**, 17–24.

Benning, L.G. & Seward, T.M. 1996. Hydrosulfide complexing of Au(I) in hydrothermal solutions from 150 to 400°C and 500 to 1500 bars. *Geochimica et Cosmochimica Acta* **60**, 1849–1871.

Bi, X., Hu, R. & Cornell, D.H. 2004. The alkaline porphyry associated Yao'an gold deposit, Yunnan, China: rare earth element and stable isotope evidence for magmatic-hydrothermal ore formation. *Mineralium Deposita* **39**, 21–30.

Bierlein, F.P., Waldron, H.M. & Arne, D.C. 1999. Behaviour of rare earth and high field strength elements during hydrothermal alteration of meta-turbidites associated with mesothermal gold mineralization in central Victoria, Australia. *Journal of Geochemical Exploration* **67**, 109–125.

Bingöl, E. & Delaloye, M. 2000. Granitoids from western and northwestern Anatolia: geochemistry and modeling of geodynamic evolution. *International Geology Reviews* **42**, 241–268.

Bingöl, E., Delaloye, M. & Ataman, G. 1982. Granitic intrusions in western Anatolia: a contribution to the geodynamic study of this area. *Eclogae Geologicae Helvetiae* **75**, 437–446.

Bischoff, J.L. & Rosenbauer, R.J. 1985. An empirical equation of state for hydrothermal seawater (3.2 percent NaCl). *American Journal of Science* **285**, 725–763.

Bodnar, R.J. 1993. Revised equation and table for determining the freezing point depression of H_2O NaCl solutions. *Geochimica Cosmochimica Acta* **57**, 683–684.

Bodnar, R.J. 2003. Introduction to fluid inclusions. *In:* Samson, I., Anderson, A. & Marshall, D. (eds), *Fluid Inclusions: Analysis and Interpretation*. Mineralogical Association of Canada Short Course **32**, 374 p.

Bodnar, R.J., Reynolds, T.J. & Kuehn, C.A. 1985. Fluid inclusion systematics in epithermal systems. *In:* Berger, B.R. & Bethke, P.M. (eds), *Geology and Geochemistry of Epithermal Systems: Reviews in Economic Geology* **2**, 73–98.

Browne, P.R.L. 1978. Hydrothermal alteration in active geothermal fields. *Annual Review of Earth and Planetary Science* **6**, 229–250.

Brill, B.A. 1988. Illite crystallinity, b_0 and Si content of K-white mica as indicators of metamorphic conditions in low-grade metamorphic rocks at Cobar, New South Wales. *Australian Journal of Earth Sciences* **35/3**, 295–302.

Cebula, G.T., Kunk, M.J., Mehnert, H.H., Naeser, J.D., Obradovich, J.D. & Sutter, J.F. 1986. The Fish Canyon Tuff, a potential standard for the $^{40}Ar/^{39}Ar$ and fission-track dating methods. *Terra Cognita* **6**, 139–140.

Çiftçi, N.B. & Bozkurt, E. 2009. Pattern of normal faulting in the Gediz Graben, SW Turkey. *Tectonophysics* **473**, 234–263.

Çolakoğlu, A.R. 2000. The characteristics of Küçükdere epithermal (Havran-Balıkesir) gold vein. *Geological Bulletin of Turkey* **43**, 99–110.

Cole, D.R. & Drummond, S.E. 1986. The effect of transport and boiling on Ag/Au ratios in hydrothermal solutions: a preliminary assessment and possible implications of the formation of epithermal precious-metal ore deposits. *Journal of Geochemical Exploration* **25**, 45–79.

Cooke, D.R. & Bloom, M.S. 1990. Epithermal and subjacent porphyry mineralization, Acupan, Baguio district, Philippines: a fluid inclusion and paragenetic study. *Journal of Geochemical Exploration* **35**, 297–340.

Cooke, D.R. & Simmons, S.R. 2000. Characteristics and genesis of epithermal gold deposits. *Reviews in Economic Geology* **13**, 221–244.

Corbett, G.J. & Leach, T.M. 1998. High sulfidation gold-copper systems in South Pacific Rim gold-copper systems: structure, alteration, and mineralization. *Society of Economic Geologists Special Publication* **6**, 101–136.

Crawford, M.L. 1981. Phase equilibria in aqueous fluid inclusions. *In:* Hollister, L.S. & Crawford, M.L. (eds), *Fluid Inclusions: Applications to Petrology*. Mineralogical Association of Canada, Short Course Handbook **6**, 75–100.

Davis, D.W., Lowenstein, T.K. & Spencer, R.J. 1990. Melting behavior of fluid inclusions in laboratory-grown halite crystals in the systems NaCl-H_2O, NaCl-KCl-H_2O, NaCl-$MgCl_2$-H_2O, and NaCl-$CaCl_2$-H_2O. *Geochimica et Cosmochimica* Acta **54**, 591–601.

Delaloye, M. & Bingöl, E. 2000. Granitoids from western and northwestern Anatolia: geochemistry and modeling of geodynamic evolution. *International Geological Review* **42**, 241–268.

Dilek, Y. & Altunkaynak, S. 2007. Cenozoic crustal evolution and mantle dynamics of post-collisional magmatism in Western Anatolia. *International Geology Review* **49**, 431–453.

Dong, G., Morrison, G. & Jairpeth, S. 1995. Quartz textures in epithermal veins, Queensland: classification, origin, and implication. *Economic Geology* **90**, 1841–1856.

Eberl, D.D. & Velde, B. 1989. Beyond the Kubler index. *Clay Minerals* **24**, 571–577.

Echavarria, E., Nelson, E. & Humphry, J. 2006. Geologic evolution of the Caylloma Epithermal Vein District, Southern Peru. *Economic Geology* **101**, 843–863.

Ercan, T., Satır, M., Stenitz, G., Dora, A., Sarıfakıoğlu, E., Adis, C., Walter, H.J. & Yıldırım, T. 1995. Biga yarimadasi ile Gokceada, Bozcaada ve Tavsan adalarindaki (KB Anadolu) Tersiyer volkanizmasinin ozellikleri. *Maden Tetkik ve Arama Enstitusu Dergisi* **117**, 55–86 (in Turkish with English abstract).

Ercan, T., Türkecan, A., Akyürek, B., Günay, E., Çevikbaş, A., Ateş, M., Can, B., Erkan, M. & Özkirişçi, E. 1984. The geology of Dikili-Bergama-Çandarlı area (western Anatolia) and petrology of the magmatic rocks. *Jeoloji Mühendisliği Dergisi* **20**, 47–60 (in Turkish with English abstract).

Erkül, F. 2004. Early Miocene Volcanism within the Bigadiç Borate Basin: Evidence for Transition from Compressional to Extensional Regime in Western Turkey. PhD Thesis, Dokuz Eylül University, İzmir-Turkey.

Erkül, F., Helvacı, C. & Sözbilir, H. 2005a. Evidence for two episodes of volcanism in the Bigadiç borate basin and tectonic implications for western Turkey. *Geological Journal* **40**, 545–570.

Erkül, F., Helvacı, C & Sözbilir, H. 2005b. Stratigraphy and geochronology of the Early Miocene volcanic units in the Bigadiç Borate Basin, Western Turkey. *Turkish Journal of Earth Sciences* **14**, 227–253.

Ersoy, Y. & Helvacı, C. 2007. Stratigraphy and geochemical features of the Early Miocene bimodal (ultrapotassic and calc-alkaline) volcanic activity within the NE-trending Selendi basin, Western Anatolia, Turkey. *Turkish Journal of Earth Sciences* **16**, 117–139.

Etoh, J., Izawa, E. & Watanbe, K. 2002. Bladed quartz and its relationship to gold mineralization in the Hishikari low-sulfidation epithermal gold deposit, Japan. *Economic Geology* **97**, 1841–1851.

Fournier, R.O. 1985. The behavior of silica in hydrothermal solutions. *Reviews in Economic Geology* **2**, 45–61.

Genç, S.C. 1998. Evolution of the Bayramiç magmatic complex, northwestern Anatolia. *Journal of Volcanology and Geothermal Research* **85**, 233–249.

Goldstein, R.H. 2003. Introduction to fluid inclusions. *In:* Samson, I., Anderson, A. & Marshall, D. (eds), *Fluid Inclusions: Analysis and Interpretation*. Mineralogical Association of Canada Short Course **32**, 374 p.

Goldstein, R.H. & Reynolds, T.J. 1994. Systematics of Fluid Inclusions in Diagenetic Minerals: Society of Economic Geologists and Paleontologists Short Course **31**, 199 p.

Hasözbek, A., Erdoğan, B., Satır, M., Siebel, W., Akay, E., Doğan, G.D. & Taubold, H. 2012. Al-in-hornblende thermobarometry and Sr-Nd-O-Pb isotopic compositions of the Early Miocene Alaçam granite in NW Anatolia (Turkey). *Turkish Journal of Earth Sciences* **21**, 37–52.

Hasözbek, A., Satır, M., Erdoğan, B., Akay, E. & Siebel, W. 2010. Early Miocene post-collisional magmatism in NW Turkey: geochemical and geochronological constraints. *International Geology Review* **53/9**, 1098–1119.

Hedenquist, J.W., Arribas, A. & Gonzales-Urien, E. 2000. Exploration for epithermal gold. *In:* Hagemann, S.G. & Brown, P.E. (eds), *Gold in 2000. Reviews in Economic Geology* **13**, 245–277.

Hedenquist, J.W. & Henley, R.W. 1985. The importance of CO_2 on freezing point measurements of fluid inclusions: evidence from active geothermal systems and implications for epithermal ore deposition. *Economic Geology* **80**, 1379–1406.

Hedenquist, J.W., Reyes, A.G., Simmons, S.F. & Taguchi, S. 1992. The thermal and geochemical structure of geothermal and epithermal systems: a framework for interpreting fluid inclusion data. *European Journal of Mineralogy* **4**, 989–1015.

Heinrich, C.A., Driesner, T., Stefansson, A. & Seward, T.M. 2004. Magmatic vapor contraction and the transport of gold from the porphyry environment to epithermal ore deposits. *Geological Society of America Bulletin* **32**, 761–764.

Henley, R.W. & Ellis, A.J. 1983. Geothermal systems ancient and modern: a geochemical review. *Earth Science Reviews* **19**, 1–50.

Henley, R.W. & Hedenquist, J.W. 1986. Introduction to the geochemistry of active and fossil geothermal systems. *In:* Henley, R.W., Hedenquist, J.W., Roberts, P.J. (eds), *Guide to the Active Epithermal Systems and Precious Metal Deposits of New Zealand*. Monography Series Mineral Deposits **26**, 129–145.

Henning, D., Lehmann, B., Burgess, R. & Tak, M.A.N. 2008. Geology, geochemistry and $^{40}Ar/^{39}Ar$ ages of the Cerro Millo epithermal high-sulfidation gold prospect, southern Peru. *Ore Geology Reviews* **34**, 304–316.

Hosono, T. & Nakano, T. 2003. Petrochemistry of volcanic rocks in the Hishikari mining area of southern Japan, with implications for the relative contribution of lower crust and mantle-derived basalt. *Resource Geology* **53**, 239–259.

Karacık, Z. & Yılmaz, Y. 1998. Geology of the ignimbrites and the associated volcano-plutonic complex of the Ezine Area, northwestern Anatolia. *Journal of Volcanology and Geothermal Research* **85**, 251–264.

Marchev, P., Singer, B.S., Jelev, D., Hasson, S., Moritz, R. & Bonev, N. 2004. The Ada Tepe deposit: a sediment-hosted, detachment fault controlled, low-sulfidation gold deposit in the Eastern Rhodopes, SE Bulgaria. *Schweizerische Mineralogische und Petrographische Mitteilungen* **84**, 59–78.

Matsuhisa, Y., Goldsmith, J.R. & Clayton, R.N. 1979. Oxygen isotopic fractionation in the system quartz-albite-anorthite-water. *Geochimica et Cosmochemica Acta* **43**, 1131–1140.

McInnes, B.I.A., Crocket, J.H. & Goodfellow, W.D. 1990. The Laforma deposit, an atypical epithermal-Au system at Free Gold Mountain, Yukon Territory, Canada. *Journal of Geochemical Exploration* **36**, 73–102.

McKenzie, D. & Yılmaz, Y. 1991. Deformation and volcanism in western Turkey and Aegean. *Bulletin of the Technical University of Istanbul* **44**, 345–373.

Nakamura, N. 1974. Determination of REE, Ba, Fe, Mg, Na and K in carbonaceous and ordinary chondrites. *Geochimica et Cosmochimica Acta* **38**, 757–773.

Okay, Ü.A. & Göncüoğlu, M.C. 2004. The Karakaya Complex: a review of data and concepts. *Turkish Journal of Earth Sciences* **13**, 77–95.

Oygur, V. 1997. Anatomy of an epithermal mineralization: Mumcu (Balikesir-Sındırgı), inner-Western Anatolia, Turkey. *Mineral Research Exploration Bulletin* **119**, 29–39.

Palacios, C.M., Hein, U.F. & Dulski, P. 1986. Behavior of rare earth elements during hydrothermal alteration at the Buena Esperanza copper–silver deposit, north Chile. *Earth and Planetary Science Letters* **80**, 208–216.

Pirajno, F. 1995. Volcanic-hosted epithermal systems in northwest Turkey. *South African Journal Geology* **98**, 13–24.

Potter, R.W. 1977. Pressure corrections for fluid-inclusion homogenization temperatures based on the volumetric properties of the system NaCl-H_2O. *Journal of Research of the U. S. Geological Survey* **5**, 603–607.

Reyes, A.G. 1990. Petrology of Philippine geothermal systems and the application of alteration mineralogy to their assessment. *Journal of Volcanology and Geothermal Research* **43**, 279–309.

Roedder, E. 1984. *Fluid Inclusions: Reviews in Mineralogy* **12**, Mineralogical Society of America.

Roedder, E. & Bodnar, R.J. 1980. Geologic pressure determinations from fluid inclusion studies. *Annual Review of Earth and Planetary Sciences* **8**, 263–301.

Ruggieri, G., Cathelineau, M., Oiron, M.C. & Marignac, C. 1999. Boiling and fluid mixing in the chlorite zone of the Larderello geothermal system. *Chemical Geology* **154**, 237–256.

Scott, M. & Watanabe, A.Y. 1998. Extreme boiling model for variable salinity of the Hokko low-sulfidation epithermal Au prospect, southwestern Hokkaido, Japan. *Minerallium Deposita* **33**, 568–578.

Şener, A.K., Menteş, B., Sarı, R., Saygılı, A. & Tufan, V. 2006. Geological synthesis of epithermal gold deposits in the Sındırgı district, Balıkesir Province, Western Turkey. *In*: Cook, N.J., Özgenc, İ. & Oyman, T. (eds), *Au-Ag-Te-Se Deposits, Proceedings of 2006 Workshop of IGCP-486*, İzmir, Turkey, 148–153.

Şener, A.K., Tufan, V., Sarı, R. & Kaplan, E.H. 2006. Sındırgı Gold Project, Galata Madencilik, Turkey Company Report, 1–20 [unpublished].

Seward, T.M. & Barnes, H.L. 1997. Metal transport by hydrothermal ore fluids. *In:* Barnes, H.L. (ed), *Geochemistry of Hydrothermal Ore Deposits*, 3rd ed. John Wiley and Sons, New York, 435–486.

Seyitoğlu, G. 1997. The Simav Graben: an example of young E-W trending structures in the Late Cenozoic extensional system of western Turkey. *Turkish Journal of Earth Sciences* **6**, 135–141

Seyitoğlu, G., Anderson, D., Nowell, G. & Scott, B. 1997. The evolution from Miocene potassic to Quaternary sodic magmatism in Western Turkey: implications for enrichment processes in lithospheric mantle. *Journal of Volcanology and Geothermal Research* **76**, 127–147.

Seyitoğlu, G. & Scott, B. 1991. Late Cenozoic crustal extension and basin formation in west Turkey. *Geological Magazine* **128**, 155–166.

Shamanian, G.H., Hedenquist, J.H., Hattori, K.H. & Hassanzadeh, J. 2004. The Gandy and Abolhassani epithermal prospects in the Alborz Magmatic Arc, Semnan province, northern Iran. *Economic Geology* **99**, 691–712.

Sharp, Z.D. 1990. A laser-based microanalytical method for the in situ determination of oxygen isotope ratios of silicates and oxides. *Geochimica et Cosmochimica Acta* **54**, 1353–1357.

Shepherd, T.J., Rankin, A.H. & Alderton, D.H.M. 1985. A Practical Guide to Fluid Inclusion Studies. London, Chapman & Hall.

Sherlock, R.L. 2005. The relationship between the McLaughlin gold–mercury deposit and active hydrothermal systems in the Geysers–Clear Lake area, northern Coast Ranges, California. *Ore Geology Reviews* **26**, 349–382.

Simmons, S.F. 1991. Hydrothermal implications of alteration and fluid inclusion studies in the Fresnillo district, Mexico: evidence for a brine reservoir and a descending water table during the formation of hydrothermal Ag-Pb-Zn orebodies. *Economıc Geology* **86**, 1579–1601.

Simmons, S.F., Arehart, G., Simpson, M.P. & Mauk, J.L. 2000. Origin of massive calcite veins in the Golden Cross low-sulfidation epithermal Au-Ag deposit, New Zealand. *Economic Geology* **95**, 99–112.

Simmons, S.F. & Brown, P.R.L. 1997. Saline fluid inclusions in sphalerite from the Broadlands-Ohaaki geothermal system: a coincidental trapping of fluids boiled towards dryness. *Economic Geology* **92**, 485–489.

Simmons, S.F. & Brown. P.R.L. 2000. Hydrothermal minerals and precious metals in the Broadlands-Ohaaki geothermal system: implications for understanding low-sulfidation epithermal environments. *Economic Geology* **95**, 971–999.

Simmons, S.F. & Christenson, B.W. 1994. Origins of calcite in a boiling geothermal system. *American Journal of Science* **294**, 361–400.

Simmons, S.F., White, N.C. & John, D.A. 2005. Geological characteristics of epithermal precious and base metal deposits. *Economic Geology 100th Anniversary Volume*, 485–522.

Staudacher, T.H., Jessberger, E.K., Dorflinger, D. & Kiko, J. 1978. A refined ultrahigh-vacuum furnace for rare gas analysis. *Journal of Physics E: Scientific Instruments* **11**, 782–784.

Stefannsson, A., Arnorsson, S. & Bjarnason, J.O. 2007. Fluid-fluid interactions in geothermal systems. *Reviews in Mineralogy and Geochemistry* **65**, 259–312

Steven, T.A., Mehnert, H.H. & Obradovich, J.D. 1978. Age of volcanic activity in the San Juan Mountains, Colorado. *U.S. Geological Survey Professional Paper* **575-D**, 47–55.

Tokçaer, M., Agostini, S. & Savaşçın, M.Y. 2005. Geotectonic setting and origin of the youngest Kula volcanics (western Anatolia), with a new emplacement model. *Turkish Journal of Earth Sciences* **14**, 143–166.

Wendt, I. & Carl, C. 1991. The statistical distribution of the mean squared weighted deviation. *Chemical Geology* **86**, 275–285.

White, N.C. & Hedenquist, J.W. 1995. Epithermal gold deposits: styles, characteristics and exploration. *SEG Newsletter* **27**, 1–13.

Wilkinson, J.J. 2001. Fluid inclusions in hydrothermal ore deposits. *Lithos* **55**, 229–272.

Yiğit, O. 2006. Gold in Turkey—a missing link in Tethyan metallogeny. *Ore Geology Reviews* **28**, 147–179.

Yiğit, O. 2009. Mineral deposits of Turkey in relation to Tethyan metallogeny: implications for future mineral exploration. *Economic Geology* **104**, 19–51.

Yılmaz, H. 1992. Turkey Regional Project. EuroGold, Turkey. Unpublished company report, 20 pp.

Yılmaz, H. 2002. Ovacık gold deposit - an example of quartz-adularia-type gold mineralization in Turkey. *Economic Geology* **97**, 1829–1839.

Yılmaz, H. 2004. Ovacık gold deposit - an example of quartz-adularia-type gold mineralization in Turkey. *In*: Cook, N.J. (ed), *Au-Ag-Te-Se Deposits, Proceedings of 2004 Workshop of IGCP-486*. Alba Julia, Romania, 148–153 (extended abstract).

Yılmaz, Y. 1989. An approach to the origin of young volcanic rocks of western Turkey. *In:* Şengör, A.C.M. (ed), *Tectonic Evolution of the Tethyan Region*. Kluwer Academic Publications, The Hague, 159–189.

Yılmaz, Y., Genç, S.C., Gürer, O.F., Bozcu, M., Yılmaz, K., Karacık, Z., Altunkaynak, S. & Elmas, A. 2000. When did the western Anatolian graben begin to develop? *In*: Bozkurt, E., Winchester, J.A. & Piper, J.D.A. (eds), *Tectonics and Magmatism in Turkey and the Surrounding Area, Geological Society Special Publication* **173**. Geological Society, London, 353–384.

Yılmaz, Y., Genç, S.C., Karacık, Z. & Altunkaynak, S. 2001. Two contrasting magmatic association of NW Anatolia and tectonic significance. *Journal of Geodynamics* **31**, 243–271

Yılmaz, Y. & Karacık, Z. 2001. Geology of the northern side of the Gulf of Edremit and its tectonic development of the Aegean graben. *Geodinamica Acta* **14**, 31–43.

Yılmaz, H., Oyman, T., Arehart, G.B., Çolakoğlu, A.R. & Billor, Z. 2007. Low-sulfidation type Au-Ag mineralization at Bergama, Izmir, Turkey. *Ore Geology Reviews* **32**, 81–124.

Yılmaz, H., Oyman, T., Sönmez, F.N., Arehart, G.B. & Billor, Z. 2010. Intermediate sulfidation epithermal gold-base metal deposits in tertiary subaerial volcanic rocks, Şahinli/Tespih Dere (Lapseki/Western Turkey). *Ore Geology Reviews***.**

Zanchi, A., Kissel, C. & Tıpırdamaz, C. 1990. Continental deformation in western Turkey: a structural and paleomagnetic approach. *International Earth Science Congress on Aegean Regions*, Dokuz Eylül University, İzmir, Turkey, 357–367.

Zanchi, A., Kissel, C. & Tıpırdamaz, C. 1993. Late Cenozoic and quaternary brittle continental deformation in western Turkey. *Bulletin Sociéte Geologique de France* **164**, 507–517.

Zhai, W., Sun, X., Sun, W., Su, L., He, X. & Wu, Y. 2009. Geology, geochemistry, and genesis of Axi: a Paleozoic low-sulfidation type epithermal gold deposit in Xinjiang, China. *Ore Geology Reviews* **36**, 265–281.